The Astrophysical Journal, 710:1142–1169, 2010 February 20 doi:10.1088/0004-637X/710/2/1142

SpeX SPECTROSCOPY OF UNRESOLVED VERY LOW MASS BINARIES. I. IDENTIFICATION OF 17 CANDIDATE BINARIES STRADDLING THE L DWARF/T DWARF TRANSITION

Adam J. Burgasser[1,2,9], Kelle L. Cruz[3,9,10], Michael Cushing[4,11], Christopher R. Gelino[5], Dagny L. Looper[4,9], Jacqueline K. Faherty[6,7], J. Davy Kirkpatrick[5,9], and I. Neill Reid[8,9]

[1] Center for Astrophysics and Space Science, University of California San Diego, La Jolla, CA 92093, USA; aburgasser@ucsd.edu
[2] Massachusetts Institute of Technology, Kavli Institute for Astrophysics and Space Research, Building 37, Room 664B, 77 Massachusetts Avenue, Cambridge, MA 02139, USA
[3] Astronomy Department, California Institute of Technology, Pasadena, CA 91125, USA
[4] Institute for Astronomy, University of Hawaii, 2680 Woodlawn Drive, Honolulu, HI 96822, USA
[5] Infrared Processing and Analysis Center, California Institute of Technology, Pasadena, CA 91125, USA
[6] Department of Astrophysics, American Museum of Natural History, Central Park West at 79th Street, New York, NY 10034, USA
[7] Department of Physics and Astronomy, Stony Brook University, Stony Brook, NY 11794-3800, USA
[8] Space Telescope Science Institute, 3700 San Marin Drive, Baltimore, MD 21218, USA
Received 2009 June 16; accepted 2010 January 5; published 2010 January 27

ABSTRACT

We report the identification of 17 candidate brown dwarf binaries whose components straddle the L dwarf/T dwarf transition. These sources were culled from a large near-infrared spectral sample of L and T dwarfs observed with the Infrared Telescope Facility SpeX spectrograph. Candidates were selected on the basis of spectral ratios which segregate known (resolved) L dwarf/T dwarf pairs from presumably single sources. Composite templates, constructed by combining 13,581 pairs of absolute flux-calibrated spectra, are shown to provide statistically superior fits to the spectra of our 17 candidates as compared to single templates. Ten of these candidates appear to have secondary components that are significantly brighter than their primaries over the 1.0–1.3 μm band, indicative of rapid condensate depletion at the L dwarf/T dwarf transition. Our results support prior indications of enhanced multiplicity amongst early-type T dwarfs; 53% ± 7% of the T0–T4 dwarfs in our spectral sample are found to be either resolved or unresolved (candidate) pairs, although this is consistent with an intrinsic (volume complete) brown dwarf binary fraction of only 15%. If verified, this sample of spectral binaries more than doubles the number of known L dwarf/T dwarf transition pairs, enabling a broader exploration of this poorly understood phase of brown dwarf atmospheric evolution.

Key words: binaries: general – brown dwarfs – stars: fundamental parameters – stars: low-mass

Online-only material: color figures, machine-readable tables

1. INTRODUCTION

Among the outstanding problems in brown dwarf astrophysics today is the depletion of photospheric condensate clouds at the transition between the two lowest-luminosity spectral classes of low-mass stars and brown dwarfs, the L dwarfs and T dwarfs (Kirkpatrick 2005 and references therein). The L dwarfs, with effective temperatures of 1300 K $\lesssim T_{\rm eff} \lesssim$ 2200 K (Golimowski et al. 2004), host a variety of mineral condensate species in their photospheres (Lodders 2002), as evident by their very red near-infrared colors, muted H_2O absorption bands, weak TiO and VO bands (gaseous precursors to condensates), and presence of silicate grain features (e.g., Tsuji et al. 1996; Kirkpatrick et al. 1999; Knapp et al. 2004; Cushing et al. 2006). In contrast, the cooler T dwarfs (600 K $\lesssim T_{\rm eff} \lesssim$ 1300 K), which have blue near-infrared colors and strong molecular gas absorption, appear to have relatively condensate-free atmospheres (Marley et al. 1996; Tsuji et al. 1999).

One-dimensional, static cloud models have been able to explain these trends through the confinement of condensates into cloud layers which are vertically bound by a balance of gravitational settling and vertical mixing (e.g., Ackerman & Marley 2001; Tsuji 2002; Burrows et al. 2006). In these models, the cloud layer resides at the photosphere in the L dwarfs, but sinks below the photosphere and out of view in the T dwarfs. While providing a robust, conceptual framework for understanding cloud evolution at the L dwarf/T dwarf transition, these models have nevertheless failed to explain the surprisingly narrow range of effective temperatures ($\Delta T_{\rm eff} \approx$ 200–400 K) and luminosities ($\Delta \log L_{\rm bol}/L_\odot \approx 0.3$ dex) that encompass this transition (Kirkpatrick et al. 2000; Golimowski et al. 2004; Burgasser 2007a). More remarkably, surface fluxes in the 1.0–1.3 μm region are observed to *increase* among early-type T dwarfs, the so-called "*J*-band bump" (Dahn et al. 2002; Tinney et al. 2003). Careful tuning of cloud parameters (e.g., settling efficiency, cloud coverage, or cloud top temperature) can reproduce the characteristics of the L dwarf/T dwarf transition, but in an arguably ad hoc manner (e.g., Burgasser et al. 2002b; Tsuji 2005; Cushing et al. 2008).

Binaries with L dwarf and T dwarf components have helped to clarify this transition by providing coeval, cospatial laboratories for detailed atmospheric investigations. Resolved photometry for a handful of these systems (Burgasser et al. 2006c; Liu et al. 2006; Looper et al. 2008b) have confirmed the *J*-band bump to be an intrinsic aspect of brown dwarf evolution, rather than variations in surface gravity, metallicity, or unresolved multiplicity in heterogeneous samples (Tsuji & Nakajima 2003; Burrows et al. 2006). L/T binaries have also enabled better characterization of absolute magnitude/spectral type relations across the L dwarf/T dwarf transition, confirming the narrow

[9] Visiting Astronomer at the Infrared Telescope Facility, which is operated by the University of Hawaii under Cooperative Agreement No. NCC 5-538 with the National Aeronautics and Space Administration, Science Mission Directorate, Planetary Astronomy Program.
[10] Spitzer Postdoctoral Fellow.
[11] Currently at NASA JPL, 4800 Oak Grove Dr., Mail Stop 264-723, Pasadena, CA 91109, USA.

luminosity range over which this transition occurs. Interpreted as a short timescale for the removal of condensates from brown dwarf photospheres (∼500 Myr; Burgasser 2007a), this result also explains the relative rarity of early-type T dwarfs (Metchev et al. 2008) and their high rate of multiplicity (nearly twice that of other brown dwarfs in magnitude-limited samples; Burgasser et al. 2006c; Liu et al. 2006).

Two factors conspire to hamper resolved imaging studies of L dwarf/T dwarf pairs: their low space density and corresponding greater distances from the Sun, and the inherently small physical separations of brown dwarf multiples in general (∼98% have $a \lesssim 20$ AU; e.g., Allen 2007). Fortunately, the distinct and highly structured near-infrared spectral energy distributions of L and T dwarfs makes it possible to both identify and characterize *unresolved* pairs from combined-light near-infrared spectroscopy, so-called spectral binaries. Indeed, one of the first L/T binaries found, 2MASS J0518-2828,[10] was originally identified by its peculiar near-infrared spectrum (Cruz et al. 2004), and subsequently confirmed via high angular resolution imaging with the *Hubble Space Telescope* (*HST*; Burgasser et al. 2006c). A more recent spectral binary discovery, 2MASS J0320-0446 (Burgasser et al. 2008a), was independently identified as an M8.5 + T5 spectroscopic binary with an orbital period of 0.67 yr (Blake et al. 2008). This case illustrates the increased potential of finding very closely separated systems among unresolved binaries, systems that are more amenable to astrometric and/or spectroscopic orbital mass measurements that provide critical tests of brown dwarf evolutionary theories (e.g., Zapatero Osorio et al. 2004; Liu et al. 2008; Dupuy et al. 2009). Tight binaries also have a higher probability of eclipsing (e.g., Stassun et al. 2006) and hence the potential to yield radius measurements to constrain as-yet untested structural models of evolved brown dwarfs (i.e., ages $\gtrsim$ 1 Gyr; Chabrier et al. 2009). Unresolved pairs can be identified at greater distances, enabling the construction of larger and more statistically robust samples; and provide a means of measuring the true binary fraction of brown dwarfs currently uncertain by a factor of 2–3 due to separation selection biases (e.g., Lodieu et al. 2007; Joergens 2008).

In this paper, we report the identification of 17 unresolved, L dwarf/T dwarf binary candidates selected from a large sample of low-resolution near-infrared spectra of late-type dwarfs. In Section 2, we summarize the construction and basic characteristics of the sample, including new observations of L and T dwarfs. In Section 3, we describe our method of selecting L dwarf/T dwarf binary candidates through the use of spectral indices. In Section 4, we detail our spectral template analysis technique, define metrics to assess the probability of unresolved multiplicity, and determine component parameters. In Section 5, we present the results of our spectral analysis, examining each candidate in detail. In Section 6, we discuss our results in the context of the absolute magnitude relations for L and T dwarfs, the frequency of multiples across the L dwarf/T dwarf transition, and the process of cloud depletion at this transition. The major conclusions of this study are summarized in Section 7. As Sections 2–4 are devoted to our selection and analysis techniques, readers interested primarily in the binary candidates can skip to Section 5 without loss of context.

[10] Names of sources listed in the text are shortened to [PREFIX] Jhhmm±ddmm, where [PREFIX] is the original discovery catalog: Two Micron All Sky Survey (2MASS: Skrutskie et al. 2006), Sloan Digital Sky Survey (SDSS: York et al. 2000), Deep Near-Infrared Survey of the Southern Sky (DENIS: Epchtein et al. 1997) or Infrared Proper Motion Survey (IPMS: Artigau et al. 2006), and hhmm and ±ddmm are the sexigesimal right ascension (hours and minutes) and declination (degrees and arcminutes) at equinox J2000. Full source names and coordinates are given in Tables 2, 3, and 6; additional source data can be found at the DwarfArchives site, http://dwarfarchives.org.

2. SpeX SPECTRAL SAMPLE

Our analysis is based on a large sample of low-resolution, near-infrared spectra of L and T dwarfs obtained with SpeX (Rayner et al. 2003), a low-resolution, 0.8–5.4 μm spectrograph mounted on the 3 m NASA Infrared Telescope Facility. The spectra were obtained using the prism-dispersed mode of SpeX, which provides 0.75–2.5 μm continuous wavelength coverage in a single order, with dispersion of 20–30 Å pixel^{-1} and an average resolution $\lambda/\Delta\lambda \approx 120$ for the 0.″5 slit (some sources were also observed with the 0.″8 slit). The sample is neither complete nor volume-limited; it constitutes a representative subset of ultracool dwarfs in the local disk population, based on ongoing SpeX spectroscopic follow-up by ourselves and other researchers of all known L and T dwarfs down to an effective magnitude limit of $K \approx 16$, including nearly all known L and T dwarfs within 20 parsecs of the Sun. Most of these sources observed are compiled on the Dwarf Archives Web site[11]; the SpeX spectra examined here are available at the SpeX Prism Spectral Libraries.[12]

2.1. New Observations

Ninety-nine L and T dwarfs were observed by the authors over several runs spanning 2004 September through 2008 September, as summarized in Table 1. These data were acquired in a variety of weather (clear to partly cloudy) and seeing conditions (0.″3–1.″2), but were uniformly observed using the 0.″5 or 0.″8 slit aligned at parallactic angle and generally at low air mass (sec $z \lesssim 2$). Each source was observed in multiple exposures, dithering in an ABBA pattern along the slit, with total integration times of 240–1200 s depending on source brightness and weather conditions. Nearby A0 V stars were observed for flux calibration and telluric absorption correction, and internal flat field and argon arc lamps were observed with each flux standard for pixel response and wavelength calibration. All data were reduced using the SpeXtool reduction package (Vacca et al. 2003; Cushing et al. 2004) using standard settings, as described in detail in Burgasser (2007b).

2.2. Data from the Literature

In addition to our new observations, we compiled from the literature SpeX observations of 134 L and T dwarfs with published optical and/or near-infrared spectral types spanning L3 to T8 and with data having median signal-to-noise ratios of 20 or greater over the 0.9–2.4 μm window. Those data[13] were acquired and reduced following similar procedures as described above. Combining the new and previous observations results in a sample of 253 spectra for 233 L3–T8 dwarfs.

2.3. Initial Template Sample

In order to identify and characterize unresolved binaries, we required a "clean" sample of spectral templates. An initial

[11] http://dwarfarchives.org

[12] http://www.browndwarfs.org/spexprism

[13] Data were drawn from Burgasser et al. (2004, 2006a, 2006b, 2007a, 2008a, 2008b); Cruz et al. (2004); Burgasser & McElwain (2006); Chiu et al. (2006); McElwain & Burgasser (2006); Reid et al. (2006); Burgasser (2007a, 2007b, 2007c); Liebert & Burgasser (2007); Looper et al. (2007, 2008b); Luhman et al. (2007); Siegler et al. (2007); and Sheppard & Cushing (2009).

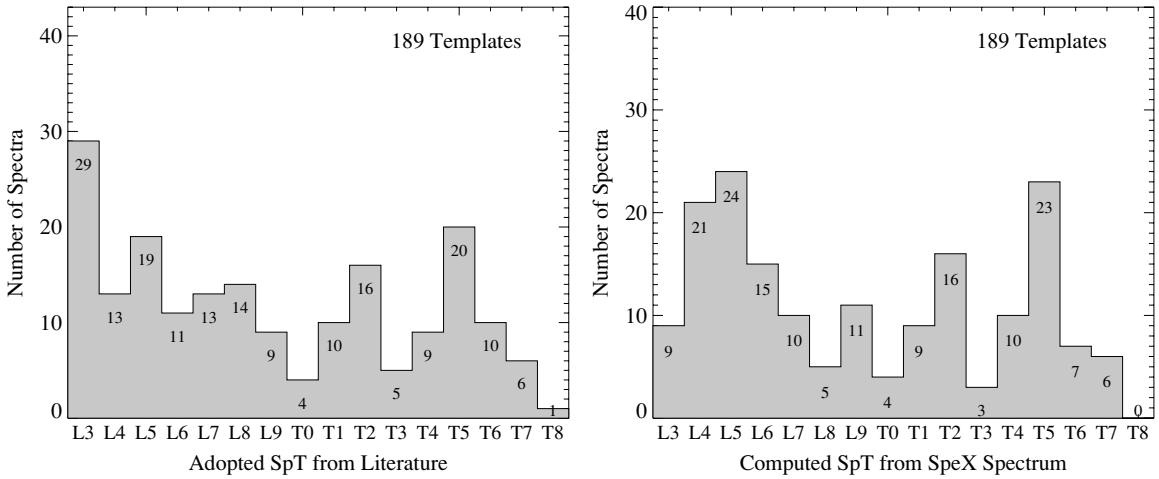

Figure 1. Distribution of spectral types for the template sample based on classifications from the literature (left) and calculated from the SpeX data (right). The former are based on optical types for L3–L8 dwarfs (where available) and near-infrared types for L9–T8 dwarfs. The distributions are roughly consistent with each other and relatively flat for the small number of sources available per subtype.

Table 1
New SpeX Spectral Observations

Source Name (1)	Opt SpT (2)	NIR SpT (3)	2MASS J (4)	UT Date (5)	Observer (6)	t_{int} (s) (7)	Slit ($''$) (8)	Air Mass (9)	Cal Star (10)
2MASS J00165953−4056541	L3.5	...	15.32 ± 0.06	2008 Sep 7	AJB	900	0.5	2.04	HD 2339
2MASS J00193927−3724392	L3:	...	15.52 ± 0.06	2003 Sep 4	KLC	720	0.8	1.26	HD 9485
2MASS J0028208+224905	...	L7:	15.61 ± 0.07	2003 Sep 3	KLC	600	0.8	1.09	HD 198070
2MASSW J0030300−145033	L7	...	16.28 ± 0.11	2007 Jul 28	DLL	960	0.5	1.22	HD 1154
SDSSp J003259.36+141036.6	...	L8	16.83 ± 0.17	2008 Jul 13	AJB	900	0.5	1.02	HD 7215
2MASSW J0051107−154417	L3.5	...	15.28 ± 0.05	2008 Sep 8	AJB	960	0.5	1.24	HD 1154
2MASS J00531899−3631102	L3.5	...	14.45 ± 0.03	2008 Sep 7	AJB	360	0.5	1.83	HD 5061
SDSSp J010752.33+004156.1	L8	L5.5	15.82 ± 0.06	2007 Oct 12	DLL	1200	0.5	1.16	HD 9485
2MASS J01311838+3801554	L4:	...	14.68 ± 0.03	2003 Sep 3	KLC	720	0.8	1.27	HD 7215
2MASS J01550354+0950003	...	L5:	14.83 ± 0.04	2003 Sep 4	KLC	360	0.8	1.05	BD+18 337A

(This table is available in its entirety in a machine-readable form in the online journal. A portion is shown here for guidance regarding its form and content.)

sample was constructed by excluding known binaries (Burgasser et al. 2007b, and references therein) young cluster objects (e.g., Muench et al. 2007), and sources specifically noted to have peculiar spectra associated with low surface gravities, subsolar metallicities or unusual cloud properties (e.g., Lucas & Roche 2000; Burgasser et al. 2003d; Knapp et al. 2004; Chiu et al. 2006; Cruz et al. 2007, 2009; Looper et al. 2008b). This left us with a sample of 189 spectra of 178 sources, whose properties are summarized in Table 2.

Figure 1 shows the distribution of published spectral types for these spectra, based on optical data for L3–L8 dwarfs or near-infrared data for L9–T8 dwarfs and those L dwarfs without optical classifications. The distribution is relatively flat, albeit with fewer T0–T3 dwarfs and T8 dwarfs reflecting the rarity of these sources in current search samples. The literature classifications are based primarily on the Kirkpatrick et al. (1999), Geballe et al. (2002), or Burgasser et al. (2006b) schemes. However, many L dwarfs have never been typed in the near-infrared, and those with near-infrared types have been classified following different schemes (e.g., Reid et al. 2001a; Testi et al. 2001; McLean et al. 2003; Nakajima et al. 2004; Burgasser 2007a). To place the sample on a self-consistent, homogeneous basis, we calculated near-infrared spectral types for each source directly from the SpeX data, using the spectral indices H_2O-J, CH_4-J, H_2O-H, CH_4-H, H_2O-K, and CH_4-K defined in Burgasser et al. (2006b) and index/spectral types relations given in Burgasser (2007a). As in the latter study, the set of indices used to classify each source is selected based on an initial (in this case, published) spectral type estimate. The H_2O-J, H_2O-H, and H_2O-K indices are combined for types L8 and earlier and the H_2O-J, CH_4-J, H_2O-H, CH_4-H, and CH_4-K indices are used for later types. As there can be significant differences between published and near-infrared spectral types, particularly for the L dwarfs (e.g., Geballe et al. 2002), we repeated the classification process three times for each source, using each iteration's classification to determine the indices used for the next iteration. The spectral type adopted for each source is the mean of its individual index types.

Table 2 lists the index-based types, with uncertainties (standard deviation of index types) given for those sources with considerable scatter (default classification uncertainty is ±0.5 subtypes). Figure 1 shows the distribution of these classifications, which is not significantly different from the literature distribution. Figure 2 compares the SpeX and literature classifications against each other. Over the entire template sample, the standard deviation between classifications is 0.9 subtypes, although average deviations are generally larger among the L dwarfs ($\sigma = 1.1$ subtypes) than the T dwarfs ($\sigma = 0.5$ subtypes). In most cases, the discrepancies are between optical and near-infrared types for L dwarfs. Only 11 sources had SpeX classifications that differed by more than two subtypes from the published classifications, one of which is a candidate binary (2MASS J1711+2232; see Section 3.2). For completeness, we used both published and index-based spectral types in our analysis.

Table 2
Spectral Templates

Source Name (1)	Opt SpT (2)	NIR SpT (3)	SpeX SpT (4)	2MASS J (5)	$J - K_s$ (6)	Reference[a] (7)
SDSS J000013.54+255418.6	...	T4.5	T4.5	15.06 ± 0.04	0.23 ± 0.13	1; 2,1
2MASSI J0013578−223520	L4	...	L3.5	15.78 ± 0.07	1.74 ± 0.08	3; 4
2MASS J00165953−4056541	L3.5	...	L4.5 ± 1	15.32 ± 0.06	1.88 ± 0.07	3; 5
2MASS J00193927−3724392	L3:	...	L3.5 ± 1	15.52 ± 0.06	1.83 ± 0.08	3; 6
2MASS J0028208+224905[d]	...	L7:	L5.0	15.61 ± 0.07	1.83 ± 0.10	3; 6
2MASSW J0030300−145033[d]	L7	...	L4.5 ± 2	16.28 ± 0.11	1.80 ± 0.15	3; 7
SDSSp J003259.36+141036.6	...	L8	L7.5	16.83 ± 0.17	1.88 ± 0.20	3; 8
2MASS J00345157+0523050	...	T6.5	T6.5	15.54 ± 0.05	< -0.71	9; 9,1
2MASSW J0036159+182110	L3.5	L4 ± 1	L4.0	12.47 ± 0.03	1.41 ± 0.03	10; 11,7,2
HD 3651B	...	T7.5	T8.0	16.16 ± 0.03	-0.71 ± 0.06	12; 13,14

Notes.
[a] Data reference followed by references for discovery, optical spectral type, and near-infrared spectral type, where available.
[b] Source satisfied one spectral index selection criterion, used as a template for spectral fitting.
[c] Source satisfied two or more spectral index selection criteria (Table 6) and not used as a template for spectral fitting.
[d] Optical, near-infrared and/or SpeX classifications deviate by two subtypes or more.
[e] Undetected in 2MASS; photometry on the Mauna Kea Observatory (MKO) system (Knapp et al. 2004).

References. (1) Burgasser et al. 2006b; (2) Knapp et al. 2004; (3) This paper; (4) Kendall et al. 2003; (5) Kirkpatrick et al. 2008; (6) K. Cruz 2010, in preparation; (7) Kirkpatrick et al. 2000; (8) Geballe et al. 2002; (9) Burgasser et al. 2004; (10) Burgasser et al. 2008a; (11) Reid et al. 2000; (12) Burgasser 2007c; (13) Mugrauer et al. 2006; (14) Luhman et al. 2007; (15) Burgasser et al. 2006a; (16) Tinney et al. 2005; (17) Cruz et al. 2004; (18) Schneider et al. 2002; (19) Cruz et al. 2007; (20) Artigau et al. 2006; (21) Liebert et al. 2003; (22) Reid et al. 2006; (23) Chiu et al. 2006; (24) Burgasser et al. 2002a; (25) Martín et al. 1999b; (26) Siegler et al. 2007; (27) Burgasser et al. 2003a; (28) Burgasser 2007a; (29) Cruz et al. 2003; (30) Looper et al. 2007; (31) Burgasser et al. 2003c; (32) Burgasser et al. 2000a; (33) Reid et al. 2008; (34) Wilson et al. 2003; (35) Gizis 2002; (36) Burgasser et al. 1999; (37) Delfosse et al. 1997; (38) Kirkpatrick et al. 1999; (39) Sheppard & Cushing 2009; (40) Leggett et al. 2000; (41) Fan et al. 2000; (42) Tsvetanov et al. 2000; (43) Burgasser et al. 2000b; (44) Burgasser et al. 2003b; (45) Gizis et al. 2000; (46) Kendall et al. 2004; (47) Metchev et al. 2008; (48) Strauss et al. 1999; (49) Kendall et al. 2007; (50) A. Burgasser 2010, in preparation; (51) Liebert & Gizis 2006; (52) Ellis et al. 2005; (53) Gizis et al. 2003; (54) Liebert & Burgasser 2007; (55) J. D. Kirkpatrick 2010, in preparation.

(This table is available in its entirety in a machine-readable form in the online journal. A portion is shown here for guidance regarding its form and content.)

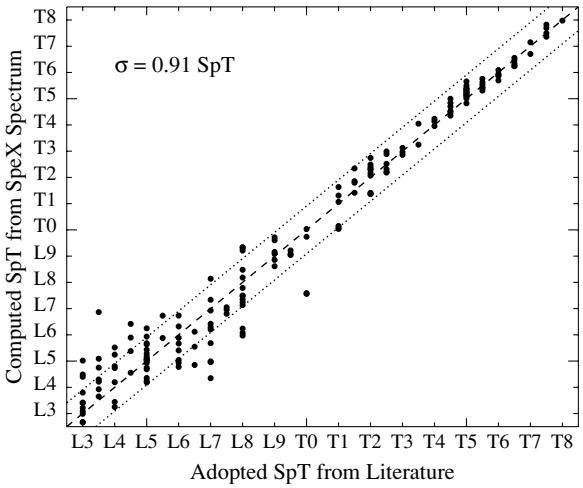

Figure 2. Comparison of spectral types from the literature and those calculated directly from the SpeX data. Overall, classifications are consistent to within 0.9 subtypes, although there is considerably more scatter among the L dwarfs ($\sigma = 1.1$) than the T dwarfs ($\sigma = 0.5$).

3. IDENTIFICATION OF BINARY CANDIDATES

3.1. Spectral Peculiarities in Known Binary Systems

Prior identification of unresolved L dwarf/T dwarf binaries from SpeX data has been based largely on the presence of peculiar spectral features, such as the sharp dip at 1.6 μm observed in the spectra of 2MASS J0320−0446, SDSS J0805+4812 (Burgasser 2007b), and Kelu-1A (Stumpf et al. 2008), attributed to overlapping FeH and CH_4 absorption features from unresolved L dwarf and T dwarf components. However, such specific features need not arise in all L/T binary combinations; see, for example, Figure 4 in Burgasser (2007a).

In an effort to make the selection process more robust, we examined the near-infrared spectra of six resolved L/T binaries (Table 3): 2MASS J0518−2828, SDSS J0423−0414 (Burgasser et al. 2005b), SDSS J1021−0304 (Burgasser et al. 2006c), 2MASS J1404+3159 (Looper et al. 2008a), SDSS J1534+1615 (Liu et al. 2006), and 2MASS J2252−1730 (Reid et al. 2006). Figure 3 compares the combined light spectrum of each of these systems to its closest match in our template library (see Section 4.2). Spectral deviations between the binaries and templates range from pronounced (in the case of 2MASS J0518−2828) to subtle (in the case of SDSS J1021-0304), but several common trends stand out.

1. The 1.6 μm CH_4 absorption band is typically stronger relative to 2.2 μm band in the binaries, the former occasionally appearing in the absence of the latter (e.g., 2MASS J0518−2828).
2. The 1.27 μm flux peak is more pronounced and H_2O and CH_4 absorption deeper at 1.1 μm in the binaries (e.g., SDSS J1534+1615).
3. The 2.1 μm flux peak is slightly shifted toward the blue in the binaries (e.g., SDSS J1021−0304).
4. The overall near-infrared spectral energy distribution is generally bluer in the binaries (e.g., 2MASS J2252−1730).

These traits suggest qualitative means of differentiating unresolved binaries from single sources, and systems such as 2MASS J0518−2828 readily stand out in direct spectral comparisons. However, comparative methods implicitly assume that the templates themselves are "normal" single spectra, an

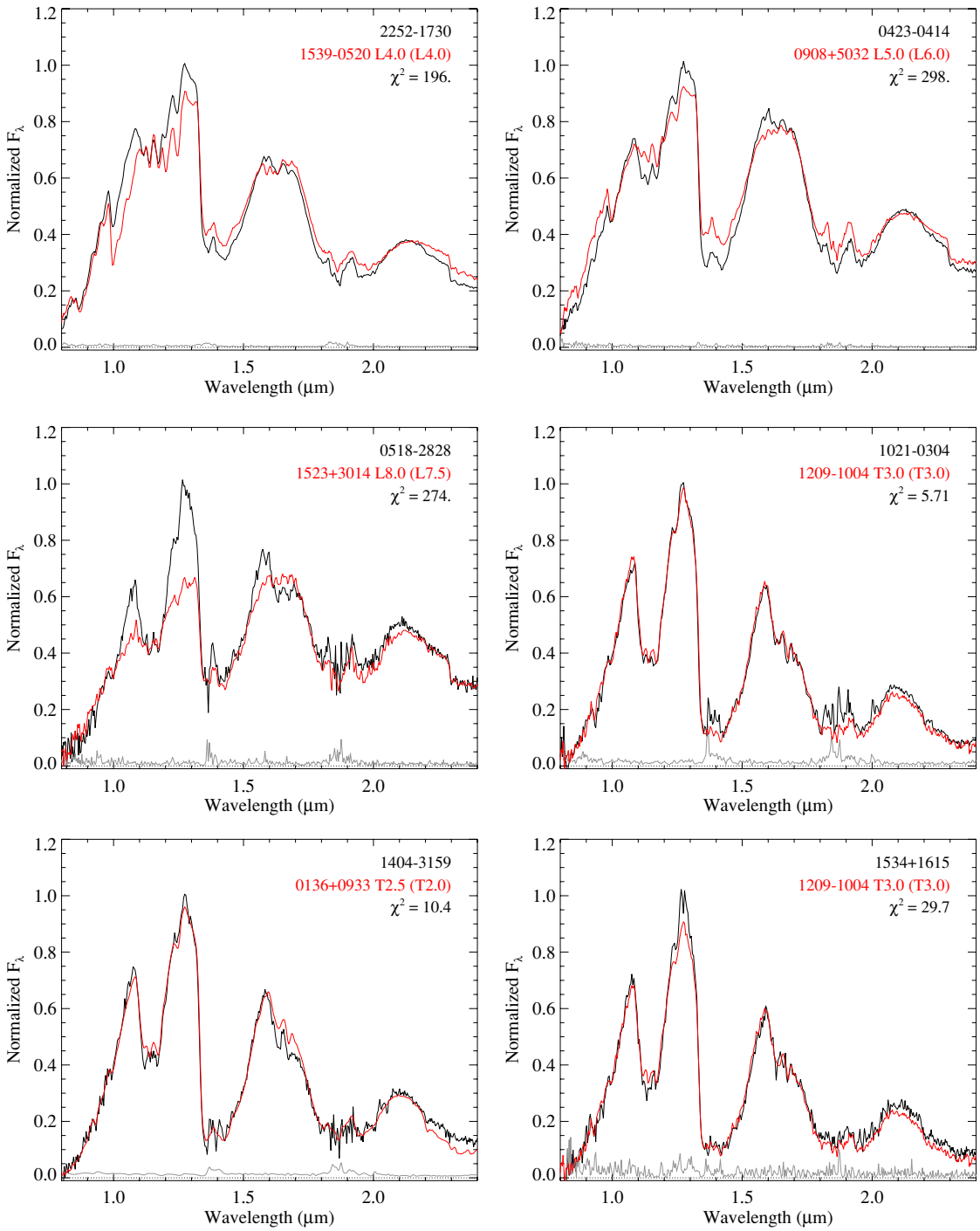

Figure 3. Comparison of known (resolved) binary spectra (Table 3; black lines) to best-fit single templates (red lines). Observed data (in F_λ flux units) have been normalized to the peak flux in the 1.0–1.3 μm range; templates are relatively normalized to minimize χ^2 deviations. Source names for both the binary and best-fit template are listed in top right corner of each panel, with both published classifications and index-based classifications (in parentheses) indicated. Also shown are the noise spectra (uncertainty in flux as a function of wavelength; gray lines) for the binaries.

(A color version of this figure is available in the online journal.)

assumption we cannot make given that we are searching for unresolved binaries within the same sample. To overcome this ambiguity, we used a suite of spectral indices to identify sources whose overall spectral properties are similar to known binaries and therefore indicative of unresolved multiplicity.

3.2. Spectral Index Selection

Eight spectral indices, defined in Table 4, were measured for each spectrum in our full spectral sample (templates and known binaries/peculiar sources). These include the six classification indices used in Section 2.2, the K/J flux peak ratio defined in Burgasser et al. (2006b), and an additional index sampling the 1.6 μm feature noted above. We compared all eight indices against each other for every source in our sample, and examined trends in individual indices and index ratios as a function of spectral type using both literature and index-based classifications.

From these combinations, we identified six pairings that best segregated known L dwarf/T dwarf binaries from the bulk of the

Table 3
Reference L Dwarf/T Dwarf Transition Binaries

Source Name	Opt SpT	NIR SpT	Component SpTs	Component Relative Magnitudes[a]		Reference
(1)	(2)	(3)	(4)	(5)		(6)
SDSSp J042348.57−041403.5	L7.5	T0	L6.5+T2	ΔF110W = 0.526 ± 0.015	ΔF170M = 0.820 ± 0.013	1
2MASS J05185995−2828372	L7.5p	T1p	L6:+T4:	ΔF110W = 0.8 ± 0.5	ΔF170M = 0.9 ± 0.6	2,3
SDSS J102109.69−030420.1	T4 ± 2	T3	T1+T5	ΔF110W = 0.06 ± 0.04	ΔF170M = 1.030 ± 0.019	3
2MASS J14044941−3159329	T0	T2.5	T1+T5	$\Delta J = -0.53 \pm 0.16$	$\Delta K = 1.20 \pm 0.21$	4
SDSS J153417.05+161546.1AB	...	T3.5	T1.5+T5.5	$\Delta J = -0.17 \pm 0.04$	$\Delta K = 1.07 \pm 0.05$	5
DENIS-P J225210.73−173013.4	...	L7.5	L6+T2	ΔF110W = 0.526 ± 0.015	ΔF170M = 0.820 ± 0.013	6

Note.
[a] Relative photometry defined as M_B–M_A; negative magnitudes indicate a secondary that is brighter than the primary. Relative JK photometry listed in the MKO system.
References. (1) Burgasser et al. 2005b; (2) Cruz et al. 2004; (3) Burgasser et al. 2006c; (4) Looper et al. 2008a; (5) Liu et al. 2006; (6) Reid et al. 2006.

Table 4
Spectral Indices

Index	Numerator Range[a]	Denominator Range[a]	Feature	Reference
(1)	(2)	(3)	(4)	(5)
H_2O-J	1.14–1.165	1.26–1.285	1.15 μm H_2O	1
CH_4-J	1.315–1.34	1.26–1.285	1.32 μm CH_4	1
H_2O-H	1.48–1.52	1.56–1.60	1.4 μm H_2O	1
CH_4-H	1.635–1.675	1.56–1.60	1.65 μm CH_4	1
H_2O-K	1.975–1.995	2.08–2.10	1.9 μm H_2O	1
CH_4-K	2.215–2.255	2.08–2.12	2.2 μm CH_4	1
K/J	2.060–2.10	1.25–1.29	$J-K$ color	1
H-dip	1.61–1.64	1.56–1.59 + 1.66–1.69[b]	1.65 μm CH_4[c]	2

Notes.
[a] Wavelength range (in μm) over which flux density (f_λ) is integrated.
[b] Denominator is sum of these two wavelength ranges.
[c] Specifically, this index samples the sharp CH_4 feature present in the near-infrared spectra of the suspected L dwarf plus T dwarf binaries 2MASS J0805+4812 (Burgasser 2007b) and Kelu-1A (Stumpf et al. 2008).
References. (1) Burgasser et al. 2006b; (2) This paper.

Table 5
Binary Index Selection Criteria[a]

Ordinate	Abscissa	Inflection Points	#[b]
(1)	(2)	(3)	(4)
H_2O-J	H_2O-K	(0.325,0.5), (0.65,0.7)	27
CH_4-H	CH_4-K	(0.6,0.35), (1,0.775)	24
CH_4-H	K/J	(0.65,0.25), (1,0.375)	28
H_2O-H	H-dip	(0.5,0.49), (0.875,0.49)	16
Spex SpT	H_2O-J/H_2O-H	(L8.5,0.925), (T1.5,0.925), (T3.5,0.85)	25
Spex SpT	H_2O-J/CH_4-K	(L8.5,0.625), (T4.5,0.825)	21

Notes.
[a] See Figure 4.
[b] Number of sources satisfying selection criteria.

spectral sample, as shown in Figure 4. These pairings reflect the peculiar traits outlined above, in particular the strength of the H-band CH_4 feature (CH_4-K versus CH_4-H and H-dip versus H_2O-H), the unusual brightness of the J-band peak (H_2O-K versus H_2O-J, H_2O-J/H_2O-H and H_2O-J/CH_4-K versus spectral type), and blue near-infrared colors (K/J versus CH_4-H). In these comparison spaces, we identified regions (Table 5) which clearly segregated known binaries, but were conservative enough so as not to over-select unusual spectra that presumably arise from non-multiplicity effects (e.g., variations in surface gravity, metallicity, or cloud properties). The criteria also allowed us to retain enough non-binary-like late-L/early-T dwarf spectra for our spectral template analysis (Section 4). These criteria clearly provide an incomplete selection of unresolved binaries, as they do not select several known binary systems with either weak signatures of CH_4 absorption (e.g., 2MASS J0850+1057 and 2MASS J1728+3948; Reid et al. 2001b; Gizis et al. 2003) or systems with identical components (e.g., SDSS J0926+584; Burgasser et al. 2006c). However, as a first attempt at identifying unresolved pairs, we chose to maximize the reliability of our candidate selection over sample completeness.

In all, 46 sources from our full SpeX sample of 253 spectra satisfied at least one selection criterion. These include nine known binaries and all six sources listed in Table 3. We refined our selection by requiring binary candidates to satisfy at least two criteria. We also segregated "strong" candidates (satisfying at least three criteria) from "weak" candidates (satisfying only two criteria), a distinction intended to test the robustness of the spectral index criteria. These 20 sources are listed in Table 6, and constitute our initial candidate pool. All have near-infrared classifications from SpeX data spanning L8.5–T3; several have been previously noted in the literature as having peculiar or highly uncertain spectral types. We discuss each candidate in detail in Section 5.

4. SPECTRAL TEMPLATE ANALYSIS

4.1. Flux Calibration

The final test of the binary nature of our candidates and characterization of their components is a comparison of their spectra against synthetic composites generated from the template spectra. The templates, purged of binary candidates (reducing the sample to 170 spectra of 161 sources), were interpolated onto a common wavelength scale and set on an absolute flux scale (in F_λ flux units) using the MKO[14] M_K/spectral type relations of Liu et al. (2006). We considered the two M_K relations defined in that study, one constructed by rejecting known binaries (hereafter, the "bright" relation) and one constructed from rejecting known and candidate binaries (hereafter, the "faint" relation; see Figure 5 in Liu et al. 2006). These two relations encompass our current best constraints on absolute magnitude trends across the L dwarf/T dwarf transition, despite diverging

[14] Mauna Kea Observatory filter system; see Tokunaga et al. (2002) and Simons & Tokunaga (2002).

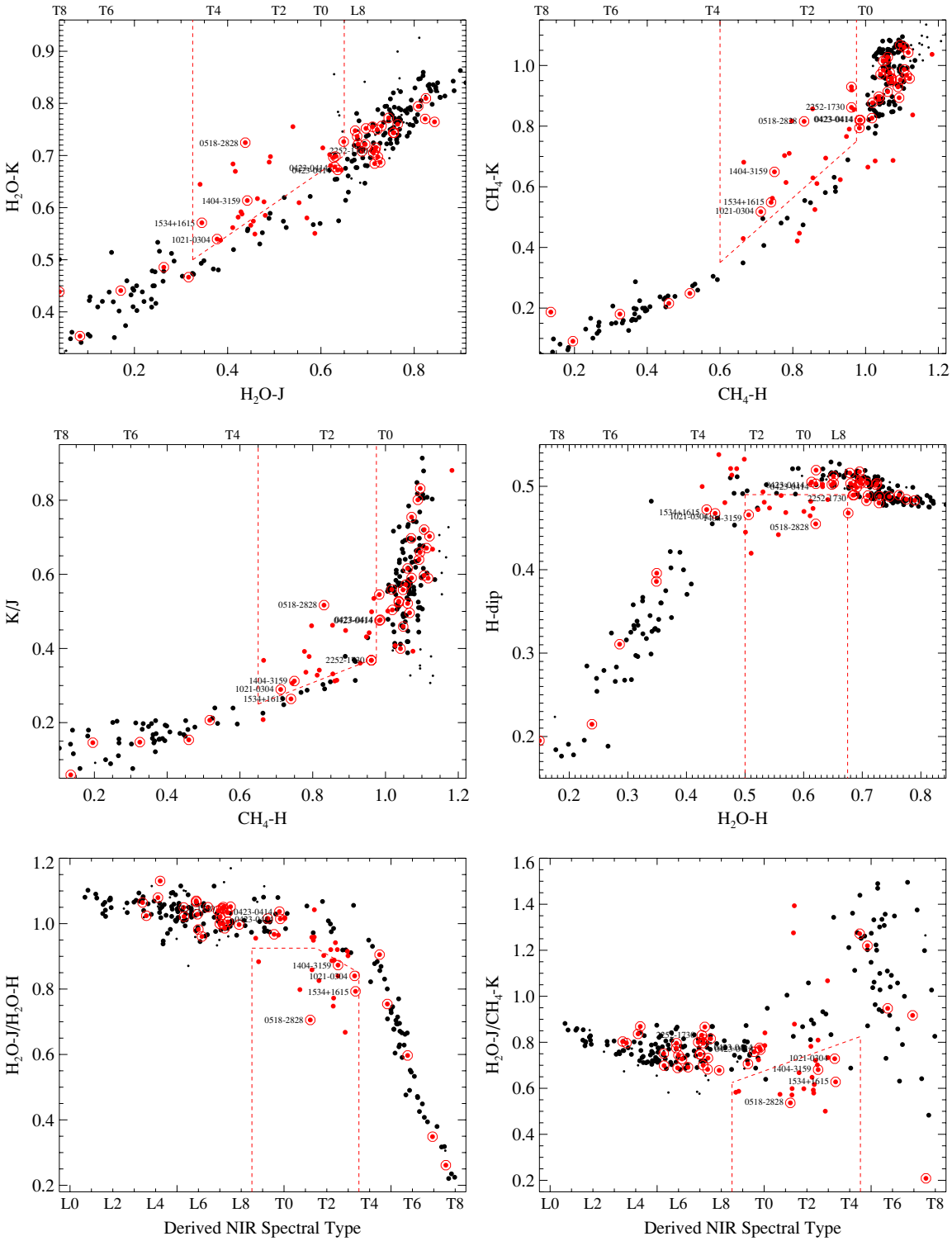

Figure 4. Spectral index selection criteria for binary candidates. Top four panels compare pairs of index values—H_2O-*K* vs. H_2O-*J*, CH_4-*K* vs. CH_4-*H*, *K*/*J* vs. CH_4-*H* and *H*-dip vs. H_2O-*H*—with estimated spectral types for each abscissa indicated at top. Bottom two panels compare index ratios H_2O-*J*/H_2O-*H* and H_2O-*J*/CH_4-*K* to near-infrared spectral type as derived from the SpeX data. In all panels, templates are indicated by large black dots, known peculiar sources by small black dots, candidate binaries by red dots and known (resolved) binaries by encircled red dots (those listed in Table 3 are also labeled). Selection spaces, with inflection points listed in Table 5, are indicated by dashed lines.

(A color version of this figure is available in the online journal.)

by nearly ∼1 mag over spectral types L8–T5. Absolute magnitudes were assigned according to either literature or index-based spectral types, resulting in four independent flux scalings for the templates. As our baseline calibration set, we adopted the faint calibration applied to literature classifications (see Section 6.1).

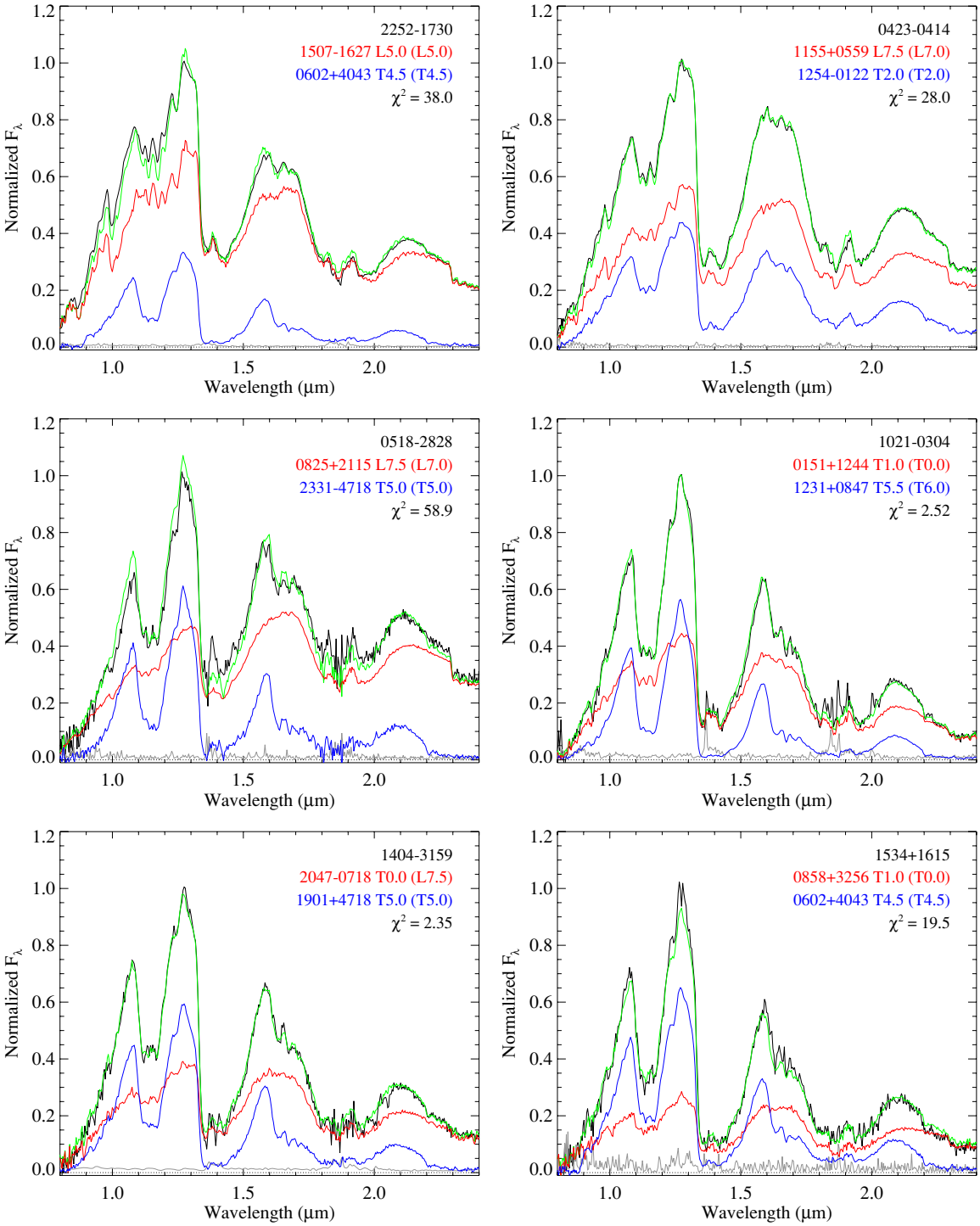

Figure 5. Best-fit composites for the resolved L dwarf/T dwarf binaries shown in Figure 3. In each panel, source spectra (black lines, in F_λ flux units) are shown normalized to the peak flux in the 1.0–1.3 μm range; composites (green lines) are relatively normalized to minimize χ^2 deviations; primary (red lines) and secondary (blue lines) component spectra are normalized to their respective contribution to the composite (based on the faint Liu et al. 2006 relation; see Section 4.1). Noise spectra for candidate data are also indicated by gray lines. Component names, literature and index-based spectral types (the latter in parentheses), and χ^2 deviations are listed in the top right corner of each panel.

(A color version of this figure is available in the online journal.)

4.2. Comparison to Single and Composites

For each candidate, we first determined best matches to individual template spectra following a procedure similar to that outlined in Burgasser et al. (2008a). All spectra were initially normalized to the maximum flux in the 1.2–1.3 μm region. We then computed a weighted χ^2 statistic between each candidate ($C[\lambda]$) and template ($T[\lambda]$) spectrum:

$$\chi^2 \equiv \sum_{\{\lambda\}} w[\lambda] \left[\frac{C[\lambda] - \alpha T[\lambda]}{\sigma_c[\lambda]} \right]^2 \quad (1)$$

(see Cushing et al. 2008). Here, $w[\lambda]$ is a vector of weights satisfying $\sum_{\{\lambda\}} w[\lambda] = 1$, α is a scaling factor that minimizes χ^2 (see Equation (2) in Cushing et al. 2008), $\sigma_c[\lambda]$ is the noise spectrum for the candidate, and the sum is performed over the wavelength ranges $\{\lambda\} = 0.95$–$1.35\ \mu$m, 1.45–1.8 μm, and 2.0–2.35 μm in order to avoid regions of strong telluric absorption. We adopted the same weighting scheme used in Cushing et al. (2008), with each pixel weighted by its spectral width (i.e., $w_i \propto \Delta\lambda_i$).

The candidate spectra were then compared to a larger set of synthetic composites, constructed by combining all possible pairs of flux-calibrated templates for which one source was of equal or later spectral type (using either literature or index-based classifications). The resulting 13,581 composites were also normalized and compared to the candidate spectra using the same χ^2 statistic as Equation (1). We note that because we are comparing the candidate spectra against a finite sample of spectra of distinct sources, each of which are modulated by some degree of noise, our expectation is not to achieve $\chi^2 \approx 1$ for our best-fit cases; indeed, this expectation is not even realized in spectral model fits (see Figure 4 in Cushing et al. 2008). What matters is whether a binary template provides a significantly improved fit, as discussed below.

4.3. Assessing Fit Quality and Parameter Estimation

The number of composites used to fit the candidate spectra vastly outnumbers the number of single templates, so we are almost assured of finding a better fit (lower χ^2) with the former. It is therefore necessary to assess the statistical significance of the fit improvement in order to rule out the null hypothesis; i.e., that the candidate is not a binary. We used the one-sided F-test for this purpose, using as our distribution statistic the ratio

$$\eta_{\rm SB} \equiv \frac{\min\left(\left\{\chi^2_{\rm single}\right\}\right)/\nu_{\rm single}}{\min\left(\left\{\chi^2_{\rm composite}\right\}\right)/\nu_{\rm binary}}, \quad (2)$$

where ν is the degrees of freedom in each fit. For both single and composite fits, one might initially assume that $\nu_{\rm single} = \nu_{\rm composite} = \nu$ is the number of data points used in the fit ($N = 296$), minus one to account for the relative scaling between data and template spectra. However, individual weighting of the spectral points implies that they do not contribute equally to the total χ^2 value. We therefore define the effective number of data points,

$$N_{\rm eff} \equiv \frac{1}{\max(\{w\})} \sum_{i=1}^{N} w_i \quad (3)$$

which reduces to N for $w_i =$ constant. For our weighting scheme, $N_{\rm eff} = 254$ and hence $\nu = 253$. To rule out our null hypothesis at the 99% confidence level (CL), we required $\eta_{\rm SB} > 1.34$ as our final selection criteria.

Typically, multiple single or composite templates yield similar χ^2 values for a given candidate. We therefore computed mean values and uncertainties for the component parameters (i.e., spectral types and relative brightnesses) using a weighting scheme based on the F-distribution. In effect, each fit's parameter set was weighted by the likelihood that that fit is equivalent to the best fit:

$$W_i \propto 1 - F(\eta_{i0} \mid \nu, \nu). \quad (4)$$

Here, $\eta_{i0} \equiv \chi^2{}_i/\min([\chi^2])$ is the ratio of χ^2 residuals between the best-fit template and the ith template, and $F(\eta_{i0} \mid \nu, \nu)$ is the F-distribution probability distribution function. Parameter means ($\bar{p}$) and uncertainties (σ_p) were then computed as

$$\bar{p} \equiv \frac{\sum_i W_i p_i}{\sum_i W_i} \quad (5)$$

and

$$\sigma_p^2 = \frac{\sum_i W_i (p_i - \bar{p})^2}{\sum_i W_i}, \quad (6)$$

where the sums are over all fits.

4.4. Known L/T Transition Binaries

Before proceeding to examine our binary candidates, we first assessed how well our index selection and spectral fitting procedures identified and reproduced the properties of the known binary systems listed in Table 3. The best-fit templates for these sources are shown in Figure 5, while Table 5 summarizes the component parameters based on the faint calibration scale. For each system, best-fit composites provided a statistically significant better match (CL > 99%) to the combined light spectrum than the best-fit single template. Visual inspection of these fits also indicates clear improvement in the cases of 2MASS J2252−1730, SDSS J0423−0414, 2MASS J0518−2828, and 2MASS J1404+3159. The fits for SDSS J1021−0304 and SDSS J1534+1615 are more subtle improvements, but notably reproduce the blueshifted peak at the K band in the spectrum of the former and the strong 1.1 μm H_2O/CH_4 band in the spectrum of the latter.

Resolved photometric measurements have been made for these systems, so we examined how well our technique reproduces reported relative magnitudes. For the composites, synthetic MKO *JHK* and *HST*/NICMOS $F110W$ and $F170M$ photometry were computed directly from the flux-calibrated SpeX data by integrating these and a Kurucz model spectrum of Vega with the respective filter profiles (see Cushing et al. 2005). Mean relative magnitudes and their uncertainties were calculated as in Equations (5) and (6), and are also listed in Table 7. In all six cases, synthetic photometry is consistent with measurements to within 2σ, although uncertainties in the former are as high as 0.8 mag. For the two sources with the most reliable photometry, SDSS J0423−0414 and 2MASS J1404+3159, the agreement is within 1.5σ.

Finally, while none of the known binaries listed in Table 3 have reported resolved spectroscopy, the inferred component types are generally consistent with estimated types from the literature (±1 subtype) with the exceptions of 2MASS J0518−2828, for which we infer later-type components (L7.5+T5 versus L6:+T4:), and DENIS J2252−1730, for which we infer an earlier primary and later secondary (L4.5+T4.5 versus L6+T2). However, reported types for the former are highly uncertain (Cruz et al. 2004; Burgasser et al. 2006c) while our spectral fit to the latter is superior to that presented in Reid et al. (2006).

In summary, we find that our method is capable of robustly identifying and characterizing known L dwarf/T dwarf transition pairs, providing a measure of confidence in our candidate binary selection and component characterization.

5. RESULTS

Single and composite template fits for each of the candidate binaries and for all four component flux calibrations are summarized in Tables 8 and 9. These include best-fit and mean

Table 6
Binary Candidates

Source (1)	Opt SpT (2)	NIR SpT (3)	SpeX SpT (4)	2MASS J (5)	$J - K_s$ (6)	Criteria (7)
Strong Candidates						
SDSS J024749.90−163112.6	...	T2 ± 1.5	T2.5 ± 1	17.19 ± 0.18	1.57 ± 0.27	6
SDSS J035104.37+481046.8	...	T1 ± 1.5	T1.5 ± 1	16.47 ± 0.13	1.47 ± 0.18	6
SDSS J103931.35+325625.5	...	T1	T1.5	16.41 ± 0.15	1.25 ± 0.22	6
2MASS J11061197+2754225	...	T2.5	T2.0	14.82 ± 0.04	1.02 ± 0.07	3
2MASS J13243559+6358284	...	T2:	T2.0 ± 1	15.60 ± 0.07	1.54 ± 0.09	3
SDSS J141530.05+572428.7	...	T3 ± 1	T3.0 ± 1	16.73 ± 0.16	<1.19	6
SDSS J143553.25+112948.6	...	T2 ± 1	T2.5 ± 1	17.14 ± 0.23	<0.23	6
SDSS J143945.86+304220.6	...	T2.5	T2.5	17.22 ± 0.23	<1.34	4
SDSS J151114.66+060742.9	...	T0 ± 2	T0.5 ± 2	16.02 ± 0.08	1.47 ± 0.13	6
SDSS J151603.03+025928.9	...	T0:	L9.5 ± 1	17.23 ± 0.20	1.80 ± 0.27	4
2MASSI J1711457+223204	L6.5	...	L9.0 ± 3	17.09 ± 0.18	2.36 ± 0.20	6
2MASS J21392676+0220226	...	T1.5	T2.5 ± 1	15.26 ± 0.05	1.68 ± 0.07	3
Weak Candidates						
SDSS J011912.22+240331.6	...	T2	T2.5	17.02 ± 0.18	< −0.02	2
SDSS J075840.33+324723.4	...	T2	T2.5	14.95 ± 0.04	1.07 ± 0.07	2
SDSS J090900.73+652527.2	...	T1.5	T1.5	16.03 ± 0.09	0.86 ± 0.17	2
2MASS J09490860−1545485	...	T2	T1.5 ± 1	16.15 ± 0.12	0.92 ± 0.20	2
SDSS J120602.51+281328.7	...	T3	T3.0	16.54 ± 0.11	<0.72	2
SDSS J120747.17+024424.8	L8	T0	T0.0	15.58 ± 0.07	1.59 ± 0.09	2
SDSS J151643.01+305344.4	...	T0.5 ± 1	T1.5 ± 2	16.85 ± 0.15	1.77 ± 0.18	2
SDSS J205235.31−160929.8	...	T1 ± 1	T0.0 ± 1	16.33 ± 0.12	1.21 ± 0.19	2

Table 7
Summary of Fits to Reference Binaries

Source	Spectral Types						
	Primary	Secondary	ΔJ	ΔK	$\Delta F110W$	$\Delta F170M$	CL[a]
(1)	(2)	(3)	(4)	(5)	(6)	(7)	(8)
SDSSp J042348.57−041403.5	L7.5 ± 0.3	T2.0 ± 0.2	0.44 ± 0.09	1.13 ± 0.07	0.59 ± 0.10	0.77 ± 0.08	>99%
2MASS J05185995−2828372	L7.5 ± 0.2	T5.0 ± 0.5	0.13 ± 0.19	2.18 ± 0.31	0.39 ± 0.20	1.71 ± 0.36	>99%
SDSS J102109.69−030420.1	T1.0 ± 0.4	T5.5 ± 0.7	0.16 ± 0.41	1.46 ± 0.29	0.37 ± 0.40	1.49 ± 0.51	>99%
2MASS J14044941−3159329	T0.0 ± 0.2	T5.0 ± 0.2	−0.27 ± 0.07	1.41 ± 0.08	−0.07 ± 0.06	1.07 ± 0.09	>99%
SDSS J153417.05+161546.1AB	T1.5 ± 0.5	T5.0 ± 1.0	0.06 ± 0.67	1.16 ± 0.47	0.23 ± 0.66	1.11 ± 0.76	>99%
DENIS-P J225210.73−173013.4	L4.5 ± 0.7	T4.5 ± 0.4	1.29 ± 0.25	2.88 ± 0.32	1.54 ± 0.25	2.50 ± 0.33	>99%

Note.
[a] Confidence limit; see Section 4.2.

component types and relative MKO *JHK* and *HST*/NICMOS $F110W$ and $F170M$ magnitudes. The best fits based on the faint flux calibration are shown in Figures 6 and 7. In the following sections, we discuss each candidate in detail.

5.1. Strong Candidates

5.1.1. SDSS J024749.90−163112.6

Originally identified in the SDSS by Chiu et al. (2006), SDSS J0247−1631 is classified T2 ± 1.5 in the near-infrared, consistent with our index-based classification of T2.5 ± 1. The uncertainty in both reflects large scatter in spectral indices, with stronger absorption in the 1.1 μm H_2O/CH_4 band relative to 1.6 and 2.2 μm CH_4 bands. SDSS J0247-1631 satisfied all six spectral index selection criteria, and the best-fit composite is a clear improvement over the single template fit and statistically significant (CL >99%). Average primary and secondary spectral types are inferred to be T0 ± 0.2 and T7 ± 0.3, the latter being the latest type secondary in our sample. The composition of this system indicates a secondary that is fainter than the primary across the near-infrared band ($\Delta J = 0.68 \pm 0.10$). The primary component of the best-fit composite, SDSS J1520+3546, has discrepant literature (T0 ± 1) and index-based (L7.5) near-infrared classifications, due in part to weak H_2O absorption at 1.1 μm and 1.3 μm; and its near-infrared color (2MASS $J - K_s = 1.54 \pm 0.08$) is somewhat blue for either type. Faherty et al. (2009) have found that unusually blue L dwarfs have a large tangential velocity (V_{tan}) distribution, indicative of older ages, higher surface gravities and possibly subsolar metallicities. SDSS J0247−1631 itself has a relatively large $V_{tan} = 46 \pm 7$ km s^{-1}, compared to a mean of 26 ± 19 km s^{-1} for L0–L9 dwarfs (Faherty et al. 2009). These characteristics suggest that SDSS J0247−1631 may be an older and/or slightly metal-poor pair of brown dwarfs. No high angular resolution imaging observations of this source have been reported to date.

5.1.2. SDSS J035104.37+481046.8

Chiu et al. (2006) classified SDSS J0351+4810 a T1 ± 1 in the near-infrared, similar to our SpeX classification (T1.5 ± 1). Again, the uncertainties arise from spectral peculiarities, in this case unusually weak CH_4 absorption at 2.2 μm. SDSS

Table 8
Template Fits to Strong Binary Candidates[a]

Mode[b] (1)	Primary (2)	Pub SpT (3)	SpeX SpT (4)	Secondary (5)	Pub SpT (6)	SpeX SpT (7)	ΔJ (8)	ΔH (9)	ΔK (10)	$\Delta F110W$ (11)	$\Delta F170M$ (12)	χ^2 (13)
SDSS J024749.90−163112.6												
Single	1750+4222	T2.0	T1.5	...	...	...	...	...	...	...	...	12.0
L06-faint	1520+3546	T0.0	L7.5	0050-3322	T7.0	T6.5	0.75	2.07	2.52	1.06	2.75	1.99
	⟨Primary⟩	T0.0 ± 0.2	L7.5 ± 0.2	⟨Secondary⟩	T7.0 ± 0.3	T6.5 ± 0.3	0.68 ± 0.10	1.96 ± 0.14	2.42 ± 0.17	0.98 ± 0.11	2.58 ± 0.24	...
L06-faint (IC)	1520+3546	T0.0	L7.5	1624+0029	T6.0	T6.0	0.50	1.75	2.44	0.78	2.23	1.70
	⟨Primary⟩	T0.0 ± 0.2	L7.5 ± 0.2	⟨Secondary⟩	T6.0 ± 0.2	T6.0 ± 0.2	0.50 ± 0.04	1.74 ± 0.05	2.42 ± 0.07	0.77 ± 0.04	2.21 ± 0.08	...
L06-bright	1520+3546	T0.0	L7.5	2356-1553	T5.5	T5.5	0.36	1.47	1.97	0.61	1.87	1.81
	⟨Primary⟩	L9.5 ± 1.1	L7.5 ± 0.9	⟨Secondary⟩	T5.5 ± 0.4	T5.5 ± 0.4	0.30 ± 0.21	1.42 ± 0.27	2.00 ± 0.23	0.55 ± 0.22	1.82 ± 0.33	...
L06-bright (IC)	1520+3546	T0.0	L7.5	1624+0029	T6.0	T6.0	0.47	1.71	2.41	0.74	2.20	1.78
	⟨Primary⟩	T0.0 ± 0.1	L7.5 ± 0.2	⟨Secondary⟩	T5.5 ± 0.4	T5.5 ± 0.3	0.43 ± 0.05	1.58 ± 0.11	2.14 ± 0.19	0.69 ± 0.06	2.00 ± 0.15	...
SDSS J035104.37+481046.8												
Single	0858+3256	T1.0	T0.0	...	...	...	...	...	...	...	...	21.3
L06-faint	0103+1935	L6.0	L6.0	0602+4043	T4.5	T4.5	0.06	1.28	2.27	0.28	1.65	6.64
	⟨Primary⟩	L6.5 ± 0.7	L6.0 ± 0.7	⟨Secondary⟩	T5.0 ± 0.7	T5.5 ± 0.6	0.31 ± 0.31	1.56 ± 0.33	2.48 ± 0.31	0.56 ± 0.32	2.00 ± 0.41	...
L06-faint (IC)	0318-3421	L7.0	L6.5	1546-3325	T5.5	T5.5	0.18	1.53	2.52	0.45	1.97	6.68
	⟨Primary⟩	L6.5 ± 1.1	L6.5 ± 0.6	⟨Secondary⟩	T5.0 ± 0.7	T5.0 ± 0.6	0.26 ± 0.30	1.51 ± 0.33	2.48 ± 0.30	0.49 ± 0.31	1.94 ± 0.41	...
L06-bright	0205+1251	L5.0	L5.5	2154+5942	T5.0	T5.5	0.21	1.49	2.37	0.43	1.93	6.55
	⟨Primary⟩	L5.5 ± 0.6	L5.5 ± 0.5	⟨Secondary⟩	T5.0 ± 0.5	T5.0 ± 0.5	0.27 ± 0.26	1.48 ± 0.28	2.38 ± 0.26	0.50 ± 0.27	1.90 ± 0.34	...
L06-bright (IC)	0205+1251	L5.0	L5.5	2124+0059	T5.0	T5.0	0.16	1.35	2.14	0.38	1.73	6.63
	⟨Primary⟩	L5.5 ± 1.0	L5.5 ± 0.6	⟨Secondary⟩	T5.0 ± 0.6	T5.5 ± 0.5	0.29 ± 0.31	1.52 ± 0.34	2.42 ± 0.32	0.53 ± 0.32	1.94 ± 0.40	...
SDSS J103931.35+325625.5												
Single	0151+1244	T1.0	T0.0	...	...	...	...	...	...	...	...	27.1
L06-faint	1043+1213	L7.0	L8.0	2254+3123	T4.0	T4.0	0.29	1.10	1.79	0.48	1.31	2.56
	⟨Primary⟩	L7.0 ± 0.2	L8.0 ± 0.2	⟨Secondary⟩	T4.0 ± 0.2	T4.0 ± 0.2	0.26 ± 0.09	1.08 ± 0.09	1.78 ± 0.08	0.46 ± 0.09	1.29 ± 0.09	...
L06-faint (IC)	1007+1930	L8.0	L9.5	1546+4932	T2.5	T3.0	−0.38	0.14	0.86	−0.27	0.29	3.42
	⟨Primary⟩	L8.0 ± 0.4	L9.0 ± 0.7	⟨Secondary⟩	T3.0 ± 0.8	T3.0 ± 0.5	−0.25 ± 0.19	0.37 ± 0.32	1.06 ± 0.34	−0.11 ± 0.23	0.53 ± 0.36	...
L06-bright	0857+5708	L8.0	L8.5	1546+4932	T2.5	T3.0	−1.09	−0.38	0.49	−0.97	−0.20	3.41
	⟨Primary⟩	L7.5 ± 0.3	L7.0 ± 1.1	⟨Secondary⟩	T2.0 ± 0.3	T3.0 ± 0.2	−1.05 ± 0.14	−0.37 ± 0.10	0.44 ± 0.07	−0.90 ± 0.13	−0.22 ± 0.09	...
L06-bright (IC)	0857+5708	L8.0	L8.5	1546+4932	T2.5	T3.0	−0.99	−0.29	0.58	−0.87	−0.11	3.24
	⟨Primary⟩	L8.0 ± 0.4	L8.0 ± 0.8	⟨Secondary⟩	T2.5 ± 0.5	T3.0 ± 0.5	−0.71 ± 0.37	−0.06 ± 0.35	0.69 ± 0.28	−0.57 ± 0.41	0.08 ± 0.33	...
2MASS J11061197+2754225												
Single	0136+0933	T2.5	T2.0	...	...	...	...	...	...	...	...	27.9
L06-faint	1520+3546	T0.0	L7.5	0000+2554	T4.5	T4.5	−0.31	0.57	1.24	−0.10	0.82	5.18
	⟨Primary⟩	T0.0 ± 0.2	L7.5 ± 0.2	⟨Secondary⟩	T4.5 ± 0.2	T4.5 ± 0.2	−0.37 ± 0.06	0.52 ± 0.07	1.16 ± 0.09	−0.16 ± 0.05	0.76 ± 0.11	...
L06-faint (IC)	2043-1551	L9.0	L9.0	0559-1404	T4.5	T4.5	−0.18	0.78	1.42	0.02	1.08	7.13
	⟨Primary⟩	L9.0 ± 0.2	L9.0 ± 0.2	⟨Secondary⟩	T4.5 ± 0.2	T4.5 ± 0.2	−0.19 ± 0.03	0.77 ± 0.05	1.43 ± 0.04	0.01 ± 0.04	1.08 ± 0.05	...
L06-bright	1520+3546	T0.0	L7.5	0559-1404	T4.5	T4.5	−0.34	0.64	1.30	−0.13	0.95	4.74
	⟨Primary⟩	T0.0 ± 0.2	L7.5 ± 0.2	⟨Secondary⟩	T4.5 ± 0.2	T4.5 ± 0.2	−0.36 ± 0.05	0.60 ± 0.08	1.26 ± 0.10	−0.15 ± 0.04	0.90 ± 0.13	...
L06-bright (IC)	1520+3546	T0.0	L7.5	0559-1404	T4.5	T4.5	−0.22	0.76	1.42	−0.01	1.07	5.98
	⟨Primary⟩	L9.5 ± 0.4	L8.0 ± 0.8	⟨Secondary⟩	T4.5 ± 0.2	T4.5 ± 0.3	−0.26 ± 0.11	0.69 ± 0.18	1.35 ± 0.16	−0.06 ± 0.13	0.99 ± 0.21	...
2MASS J13243559+6358284												
Single	0830+4828	L9.0	L9.5	...	...	...	...	...	...	...	...	32.0
L06-faint	1043+2225	L8.0	L9.0	1214+6316	T3.5	T4.0	−0.10	0.63	1.36	0.07	0.78	6.17
	⟨Primary⟩	L8.0 ± 0.2	L9.5 ± 0.2	⟨Secondary⟩	T3.5 ± 0.2	T4.0 ± 0.2	−0.05 ± 0.06	0.65 ± 0.03	1.36 ± 0.01	0.13 ± 0.07	0.80 ± 0.02	...
L06-faint (IC)	1043+2225	L8.0	L9.0	1214+6316	T3.5	T4.0	−0.21	0.53	1.25	−0.03	0.67	6.03
	⟨Primary⟩	L8.0 ± 0.2	L9.0 ± 0.2	⟨Secondary⟩	T3.5 ± 0.2	T4.0 ± 0.2	−0.20 ± 0.03	0.53 ± 0.02	1.25 ± 0.01	−0.03 ± 0.03	0.67 ± 0.01	...
L06-bright	0857+5708	L8.0	L8.5	1214+6316	T3.5	T4.0	−0.80	0.03	0.86	−0.61	0.19	8.52
	⟨Primary⟩	L8.0 ± 0.4	L8.5 ± 1.0	⟨Secondary⟩	T3.5 ± 0.9	T4.0 ± 0.9	−0.63 ± 0.41	0.15 ± 0.52	0.91 ± 0.50	−0.45 ± 0.41	0.32 ± 0.61	...
L06-bright (IC)	1043+2225	L8.0	L9.0	1214+6316	T3.5	T4.0	−0.38	0.35	1.07	−0.21	0.50	7.12
	⟨Primary⟩	L8.0 ± 0.2	L9.0 ± 0.5	⟨Secondary⟩	T3.5 ± 0.2	T4.0 ± 0.2	−0.46 ± 0.10	0.32 ± 0.06	1.09 ± 0.06	−0.28 ± 0.09	0.47 ± 0.06	...
SDSS J141530.05+572428.7												
Single	1254-0122	T2.0	T2.0	...	...	...	...	...	...	...	...	11.1
L06-faint	1523+3014	L8.0	L7.5	0741+2351	T5.0	T5.5	−0.22	1.06	1.91	0.03	1.47	1.73
	⟨Primary⟩	L8.0 ± 0.5	L8.5 ± 1.0	⟨Secondary⟩	T5.0 ± 0.3	T5.5 ± 0.2	−0.18 ± 0.12	1.07 ± 0.11	1.93 ± 0.09	0.05 ± 0.13	1.49 ± 0.13	...
L06-faint (IC)	1219+3128	L8.0	L9.5	1624+0029	T6.0	T6.0	−0.18	1.13	2.02	0.06	1.65	1.59
	⟨Primary⟩	L8.5 ± 0.8	L9.5 ± 0.2	⟨Secondary⟩	T5.5 ± 0.4	T5.5 ± 0.3	−0.28 ± 0.13	0.97 ± 0.14	1.85 ± 0.15	−0.06 ± 0.15	1.43 ± 0.18	...
L06-bright	1523+3014	L8.0	L7.5	0741+2351	T5.0	T5.5	−0.41	0.87	1.72	−0.16	1.28	1.38
	⟨Primary⟩	L8.0 ± 0.5	L7.5 ± 0.8	⟨Secondary⟩	T5.0 ± 0.2	T5.5 ± 0.2	−0.46 ± 0.13	0.83 ± 0.09	1.75 ± 0.05	−0.22 ± 0.13	1.26 ± 0.09	...
L06-bright (IC)	1219+3128	L8.0	L9.5	0741+2351	T5.0	T5.5	−0.16	1.06	1.93	0.04	1.49	1.82
	⟨Primary⟩	L8.5 ± 1.0	L9.0 ± 0.6	⟨Secondary⟩	T5.0 ± 0.3	T5.5 ± 0.3	−0.26 ± 0.25	0.96 ± 0.22	1.84 ± 0.18	−0.05 ± 0.27	1.37 ± 0.24	...
SDSS J143553.25+112948.6												
Single	1209−1004	T3.0	T3.0	...	...	...	...	...	...	...	...	42.4
L06-faint	1043+1213	L7.0	L8.0	1615+1340	T6.0	T6.0	0.48	1.89	2.66	0.71	2.44	19.9
	⟨Primary⟩	L7.5 ± 0.4	L8.0 ± 0.3	⟨Secondary⟩	T6.0 ± 0.3	T6.0 ± 0.2	0.41 ± 0.12	1.75 ± 0.23	2.51 ± 0.25	0.65 ± 0.10	2.26 ± 0.30	...
L06-faint (IC)	1520+3546	T0.0	L7.5	1615+1340	T6.0	T6.0	0.48	1.82	2.47	0.73	2.36	15.9

Table 8
(Continued)

Mode[b] (1)	Primary (2)	Pub SpT (3)	SpeX SpT (4)	Secondary (5)	Pub SpT (6)	SpeX SpT (7)	ΔJ (8)	ΔH (9)	ΔK (10)	$\Delta F110W$ (11)	$\Delta F170M$ (12)	χ^2 (13)
	⟨Primary⟩	T0.0 ± 0.6	L7.5 ± 0.2	⟨Secondary⟩	T6.0 ± 0.3	T6.0 ± 0.2	0.48 ± 0.04	1.80 ± 0.07	2.45 ± 0.08	0.72 ± 0.04	2.33 ± 0.09	...
L06-bright	1520+3546	T0.0	L7.5	1615+1340	T6.0	T6.0	0.36	1.70	2.35	0.61	2.24	16.6
	⟨Primary⟩	T0.0 ± 0.2	L7.5 ± 0.2	⟨Secondary⟩	T6.0 ± 0.2	T6.0 ± 0.2	0.36 ± 0.02	1.70 ± 0.04	2.35 ± 0.03	0.61 ± 0.02	2.24 ± 0.05	...
L06-bright (IC)	1520+3546	T0.0	L7.5	1615+1340	T6.0	T6.0	0.46	1.80	2.44	0.71	2.34	14.8
	⟨Primary⟩	L9.5 ± 0.7	L7.5 ± 0.2	⟨Secondary⟩	T6.0 ± 0.4	T6.0 ± 0.2	0.45 ± 0.02	1.77 ± 0.06	2.41 ± 0.08	0.70 ± 0.02	2.30 ± 0.09	...
SDSS J143945.86+304220.6												
Single	0136+0933	T2.5	T2.0	...	...	...	...	...	...	...	...	7.03
L06-faint	0151+1244	T1.0	T0.0	2356−1553	T5.5	T5.5	0.26	1.20	1.44	0.48	1.56	4.85
	⟨Primary⟩	T1.0 ± 0.2	T0.0 ± 0.3	⟨Secondary⟩	T5.0 ± 0.6	T5.0 ± 0.5	0.10 ± 0.17	0.95 ± 0.26	1.21 ± 0.23	0.31 ± 0.18	1.24 ± 0.33	...
L06-faint (IC)	0151+1244	T1.0	T0.0	2151−4853	T4.0	T4.0	0.03	0.74	1.10	0.23	0.90	4.37
	⟨Primary⟩	T1.0 ± 0.2	T0.0 ± 0.2	⟨Secondary⟩	T4.5 ± 0.5	T5.0 ± 0.5	0.21 ± 0.15	1.06 ± 0.26	1.35 ± 0.21	0.41 ± 0.16	1.31 ± 0.33	...
L06-bright	0151+1244	T1.0	T0.0	2151−4853	T4.0	T4.0	−0.14	0.57	0.93	0.06	0.73	4.59
	⟨Primary⟩	T1.0 ± 0.2	T0.0 ± 0.2	⟨Secondary⟩	T5.0 ± 0.6	T5.0 ± 0.6	0.24 ± 0.30	1.11 ± 0.40	1.44 ± 0.39	0.45 ± 0.31	1.38 ± 0.49	...
L06-bright (IC)	0151+1244	T1.0	T0.0	2151−4853	T4.0	T4.0	0.06	0.77	1.13	0.26	0.93	4.45
	⟨Primary⟩	T1.0 ± 0.2	T0.0 ± 0.3	⟨Secondary⟩	T4.5 ± 0.7	T5.0 ± 0.6	0.27 ± 0.31	1.12 ± 0.41	1.49 ± 0.41	0.48 ± 0.31	1.37 ± 0.51	...
SDSS J151114.66+060742.9												
Single	1030+0213	L9.5	L9.0	...	...	...	...	...	...	...	...	5.91
L06-faint	0624−4521	L5.0	L5.0	0741+2351	T5.0	T5.5	0.62	1.90	2.80	0.85	2.33	1.11
	⟨Primary⟩	L5.5 ± 0.8	L5.0 ± 0.3	⟨Secondary⟩	T5.0 ± 0.4	T5.0 ± 0.4	0.55 ± 0.26	1.78 ± 0.32	2.66 ± 0.32	0.79 ± 0.26	2.20 ± 0.37	...
L06-faint (IC)	0624-4521	L5.0	L5.0	0741+2351	T5.0	T5.5	0.78	2.06	2.96	1.01	2.49	1.29
	⟨Primary⟩	L5.5 ± 0.7	L5.0 ± 0.4	⟨Secondary⟩	T5.5 ± 0.7	T5.5 ± 0.6	0.71 ± 0.24	1.97 ± 0.30	2.94 ± 0.34	0.95 ± 0.26	2.43 ± 0.37	...
L06-bright	0624−4521	L5.0	L5.0	0516−0445	T5.5	T5.5	0.68	1.93	2.72	0.94	2.41	1.08
	⟨Primary⟩	L5.0 ± 0.3	L5.0 ± 0.4	⟨Secondary⟩	T5.5 ± 0.4	T5.5 ± 0.4	0.57 ± 0.20	1.81 ± 0.25	2.67 ± 0.26	0.81 ± 0.21	2.25 ± 0.31	...
L06-bright (IC)	0624−4521	L5.0	L5.0	1624+0029	T6.0	T6.0	0.71	2.08	2.99	0.97	2.60	1.08
	⟨Primary⟩	L5.0 ± 0.5	L5.0 ± 0.3	⟨Secondary⟩	T5.5 ± 0.6	T5.5 ± 0.5	0.60 ± 0.18	1.86 ± 0.25	2.72 ± 0.29	0.84 ± 0.18	2.30 ± 0.33	...
SDSS J151603.03+025928.9												
Single	0328+2302	L9.5	L9.0	...	...	...	...	...	...	...	...	2.85
L06-faint	0318-3421	L7.0	L6.5	1048+0919	T2.5	T2.5	−0.05	0.57	1.33	0.10	0.72	1.97
	⟨Primary⟩	L7.5 ± 1.1	L6.5 ± 1.1	⟨Secondary⟩	T2.5 ± 2.2	T2.5 ± 2.4	0.30 ± 0.65	0.87 ± 0.90	1.41 ± 1.02	0.42 ± 0.71	1.08 ± 1.17	...
L06-faint (IC)	0318−3421	L7.0	L6.5	1048+0919	T2.5	T2.5	0.07	0.69	1.45	0.22	0.84	1.98
	⟨Primary⟩	L7.5 ± 0.9	L6.5 ± 0.8	⟨Secondary⟩	T3.0 ± 2.3	T3.0 ± 2.5	0.48 ± 0.67	1.13 ± 0.96	1.74 ± 1.06	0.63 ± 0.73	1.38 ± 1.25	...
L06-bright	1044+0429	L7.0	L7.0	1217−0311	T7.5	T7.5	1.85	3.18	3.71	2.18	4.02	1.92
	⟨Primary⟩	L7.5 ± 1.3	L7.0 ± 0.8	⟨Secondary⟩	T4.0 ± 3.5	T3.5 ± 3.9	0.89 ± 0.90	1.52 ± 1.48	1.81 ± 1.80	1.03 ± 1.04	1.93 ± 1.91	...
L06-bright (IC)	1044+0429	L7.0	L7.0	0039+2115	T7.5	T8.0	1.82	3.19	3.94	2.11	4.07	1.90
	⟨Primary⟩	L7.5 ± 1.1	L7.0 ± 1.0	⟨Secondary⟩	T4.5 ± 3.3	T4.5 ± 3.7	1.00 ± 0.90	1.80 ± 1.46	2.24 ± 1.76	1.18 ± 1.03	2.29 ± 1.89	...
2MASSI J1711457+223204												
Single	0858+3256	T1.0	T0.0	...	...	...	...	...	...	...	...	3.44
L06-faint	0624−4521	L5.0	L5.0	1828−4849	T5.5	T5.5	1.01	2.21	3.02	1.23	2.64	1.49
	⟨Primary⟩	L5.0 ± 0.4	L5.5 ± 0.5	⟨Secondary⟩	T5.5 ± 1.2	T5.5 ± 1.1	0.92 ± 0.30	2.10 ± 0.48	3.05 ± 0.60	1.15 ± 0.34	2.57 ± 0.64	...
L06-faint (IC)	0624−4521	L5.0	L5.0	1346-0031	T6.5	T6.0	1.20	2.59	3.38	1.47	3.17	1.49
	⟨Primary⟩	L5.0 ± 0.8	L5.5 ± 0.7	⟨Secondary⟩	T5.5 ± 1.4	T6.0 ± 1.3	1.02 ± 0.42	2.22 ± 0.60	3.09 ± 0.67	1.26 ± 0.46	2.73 ± 0.81	...
L06-bright	0624−4521	L5.0	L5.0	1114−2618	T7.5	T7.5	1.29	2.65	4.24	1.58	3.48	1.56
	⟨Primary⟩	L5.0 ± 0.7	L5.5 ± 0.6	⟨Secondary⟩	T6.5 ± 0.8	T6.5 ± 0.8	1.19 ± 0.26	2.51 ± 0.31	3.52 ± 0.49	1.46 ± 0.27	3.13 ± 0.45	...
L06-bright (IC)	0624−4521	L5.0	L5.0	1346−0031	T6.5	T6.0	1.07	2.45	3.25	1.34	3.04	1.49
	⟨Primary⟩	L4.5 ± 0.8	L5.5 ± 0.8	⟨Secondary⟩	T6.5 ± 1.1	T6.5 ± 1.1	1.20 ± 0.38	2.47 ± 0.51	3.36 ± 0.65	1.46 ± 0.40	3.11 ± 0.73	...
2MASS J21392676+0220226												
Single	1750+4222	T2.0	T1.5	...	...	...	...	...	...	...	...	3.29
L06-faint	0830+4828	L9.0	L9.5	1214+6316	T3.5	T4.0	−0.15	0.50	1.12	0.00	0.63	1.83
	⟨Primary⟩	L8.5 ± 0.7	L9.0 ± 0.6	⟨Secondary⟩	T3.5 ± 1.0	T4.0 ± 1.0	−0.14 ± 0.21	0.62 ± 0.38	1.28 ± 0.45	0.02 ± 0.24	0.82 ± 0.47	...
L06-faint (IC)	0830+4828	L9.0	L9.5	1214+6316	T3.5	T4.0	−0.10	0.55	1.16	0.05	0.67	1.84
	⟨Primary⟩	L8.5 ± 0.7	L9.5 ± 0.4	⟨Secondary⟩	T3.5 ± 1.1	T3.5 ± 1.1	−0.21 ± 0.27	0.51 ± 0.38	1.15 ± 0.41	−0.06 ± 0.31	0.69 ± 0.45	...
L06-bright	0028+2249	L7.0	L5.0	1214+6316	T3.5	T4.0	−0.38	0.27	0.98	−0.16	0.42	1.71
	⟨Primary⟩	L8.0 ± 0.8	L8.0 ± 1.6	⟨Secondary⟩	T3.5 ± 0.8	T3.5 ± 0.9	−0.46 ± 0.26	0.19 ± 0.34	0.84 ± 0.37	−0.28 ± 0.29	0.33 ± 0.39	...
L06-bright (IC)	0830+4828	L9.0	L9.5	1214+6316	T3.5	T4.0	−0.20	0.45	1.06	−0.06	0.57	1.82
	⟨Primary⟩	L8.5 ± 1.0	L9.0 ± 0.8	⟨Secondary⟩	T3.0 ± 1.1	T3.5 ± 1.2	−0.38 ± 0.35	0.29 ± 0.49	0.91 ± 0.54	−0.23 ± 0.39	0.44 ± 0.57	...

Notes.

[a] For each source, we list the parameters of the best-fitting template (minimum χ^2) for each of the fitting modes; for the composite fits, we also give mean parameters for the primary (⟨Primary⟩) and secondary (⟨Secondary⟩), as well as the predicted relative magnitudes in the MKO *JHK* and *HST*/NICMOS $F110W$ and $F170M$ bands.

[b] Spectral fitting mode: Single: fits to single templates; L06-faint and L06-bright: fits to composite templates using the Liu et al. (2006) faint and bright M_K/spectral type relations, respectively; L06-faint (IC) and L06-bright (IC): fits to composite templates using the Liu et al. (2006) faint and bright relations, respectively, and the index-based spectral classifications.

Table 9
Template Fits to Weak Binary Candidates[a]

Mode[b] (1)	Primary (2)	Pub SpT (3)	SpeX SpT (4)	Secondary (5)	Pub SpT (6)	SpeX SpT (7)	ΔJ (8)	ΔH (9)	ΔK (10)	$\Delta F110W$ (11)	$\Delta F170M$ (12)	χ^2 (13)
SDSS J011912.22+240331.6												
Single	1254−0122	T2.0	T2.0	...	...	...	...	...	...	...	...	25.4
L06-faint	0858+3256	T1.0	T0.0	2254+3123	T4.0	T4.0	−0.60	0.08	0.83	−0.38	0.29	15.7
	⟨Primary⟩	T0.0 ± 0.7	L9.0 ± 0.9	⟨Secondary⟩	T4.0 ± 0.4	T4.5 ± 0.5	−0.42 ± 0.19	0.43 ± 0.33	1.12 ± 0.28	−0.21 ± 0.20	0.66 ± 0.37	...
L06-faint (IC)	0858+3256	T1.0	T0.0	1750+1759	T3.5	T3.0	−0.69	−0.06	0.79	−0.55	0.14	14.9
	⟨Primary⟩	T0.0 ± 1.0	T0.0 ± 0.4	⟨Secondary⟩	T4.0 ± 0.5	T3.5 ± 0.7	−0.54 ± 0.23	0.20 ± 0.39	0.99 ± 0.33	−0.39 ± 0.27	0.42 ± 0.45	...
L06-bright	0328+2302	L9.5	L9.0	2151−4853	T4.0	T4.0	−0.47	0.38	1.04	−0.26	0.58	14.2
	⟨Primary⟩	L9.0 ± 0.7	L9.0 ± 0.8	⟨Secondary⟩	T4.0 ± 0.3	T4.0 ± 0.5	−0.54 ± 0.11	0.25 ± 0.20	0.97 ± 0.16	−0.36 ± 0.16	0.46 ± 0.21	...
L06-bright (IC)	1030+0213	L9.5	L9.0	1750+1759	T3.5	T3.0	−0.71	−0.05	0.70	−0.59	0.16	13.5
	⟨Primary⟩	L9.0 ± 0.7	L9.0 ± 0.4	⟨Secondary⟩	T3.5 ± 0.2	T3.5 ± 0.3	−0.75 ± 0.16	−0.05 ± 0.19	0.73 ± 0.15	−0.63 ± 0.19	0.17 ± 0.19	...
SDSS J075840.33+324723.4												
Single	1254−0122	T2.0	T2.0	...	...	...	...	...	...	...	...	34.8
L06-faint	2047−0718	T0.0	L7.5	1214+6316	T3.5	T4.0	−0.13	0.43	0.89	0.08	0.51	47.1
	⟨Primary⟩	T0.0 ± 0.8	L9.0 ± 1.1	⟨Secondary⟩	T3.5 ± 0.8	T4.0 ± 0.6	−0.31 ± 0.25	0.32 ± 0.37	0.93 ± 0.41	−0.12 ± 0.26	0.46 ± 0.42	...
L06-faint (IC)	0151+1244	T1.0	T0.0	1214+6316	T3.5	T4.0	0.40	0.82	1.04	0.59	0.87	49.4
	⟨Primary⟩	L9.5 ± 0.9	T0.0 ± 0.2	⟨Secondary⟩	T4.0 ± 0.4	T4.0 ± 0.3	−0.12 ± 0.36	0.59 ± 0.17	1.18 ± 0.14	0.04 ± 0.38	0.78 ± 0.12	...
L06-bright	2047−0718	T0.0	L7.5	1214+6316	T3.5	T4.0	−0.25	0.31	0.77	−0.04	0.39	36.7
	⟨Primary⟩	L9.5 ± 0.6	L8.5 ± 0.8	⟨Secondary⟩	T3.5 ± 0.3	T4.0 ± 0.3	−0.28 ± 0.11	0.26 ± 0.14	0.77 ± 0.12	−0.08 ± 0.13	0.35 ± 0.14	...
L06-bright (IC)	0151+1244	T1.0	T0.0	1214+6316	T3.5	T4.0	0.40	0.81	1.03	0.58	0.87	49.4
	⟨Primary⟩	L9.5 ± 0.9	T0.0 ± 0.3	⟨Secondary⟩	T4.0 ± 0.5	T4.0 ± 0.4	−0.14 ± 0.40	0.57 ± 0.28	1.16 ± 0.24	0.03 ± 0.41	0.76 ± 0.30	...
SDSS J090900.73+652527.2												
Single	0136+0933	T2.5	T2.0	...	...	...	...	...	...	...	...	4.76
L06-faint	1750+4222	T2.0	T1.5	1048+0919	T2.5	T2.5	−0.16	−0.07	0.13	−0.16	0.00	2.53
	⟨Primary⟩	T1.5 ± 0.5	T0.5 ± 0.7	⟨Secondary⟩	T2.5 ± 0.3	T2.5 ± 0.5	−0.12 ± 0.10	0.10 ± 0.17	0.30 ± 0.19	−0.07 ± 0.11	0.17 ± 0.18	...
L06-faint (IC)	1750+4222	T2.0	T1.5	1048+0919	T2.5	T2.5	−0.06	0.03	0.24	−0.05	0.10	2.52
	⟨Primary⟩	T1.5 ± 0.5	T1.0 ± 0.6	⟨Secondary⟩	T2.5 ± 0.3	T2.5 ± 0.4	0.02 ± 0.10	0.22 ± 0.22	0.42 ± 0.25	0.07 ± 0.14	0.29 ± 0.24	...
L06-bright	1750+4222	T2.0	T1.5	1048+0919	T2.5	T2.5	−0.16	−0.07	0.13	−0.15	0.00	2.53
	⟨Primary⟩	T1.0 ± 0.8	T0.5 ± 1.1	⟨Secondary⟩	T3.0 ± 0.4	T2.5 ± 0.5	−0.20 ± 0.17	0.08 ± 0.14	0.34 ± 0.23	−0.13 ± 0.15	0.17 ± 0.16	...
L06-bright (IC)	1750+4222	T2.0	T1.5	1048+0919	T2.5	T2.5	−0.09	0.00	0.20	−0.08	0.07	2.52
	⟨Primary⟩	T1.5 ± 0.8	T0.5 ± 1.0	⟨Secondary⟩	T2.5 ± 0.4	T2.5 ± 0.5	−0.12 ± 0.18	0.15 ± 0.17	0.40 ± 0.22	−0.06 ± 0.17	0.23 ± 0.18	...
2MASS J09490860-1545485												
Single	0136+0933	T2.5	T2.0	...	...	...	...	...	...	...	...	27.2
L06-faint	1632+4150	T1.0	T1.0	1122−3512	T2.0	T2.0	−0.09	0.09	0.24	−0.07	0.15	13.7
	⟨Primary⟩	T1.0 ± 0.2	T1.0 ± 0.2	⟨Secondary⟩	T2.0 ± 0.2	T2.0 ± 0.3	−0.07 ± 0.05	0.12 ± 0.06	0.26 ± 0.05	−0.04 ± 0.06	0.18 ± 0.06	...
L06-faint (IC)	1632+4150	T1.0	T1.0	1122−3512	T2.0	T2.0	−0.09	0.09	0.24	−0.07	0.15	13.7
	⟨Primary⟩	T1.0 ± 0.2	T1.0 ± 0.2	⟨Secondary⟩	T2.0 ± 0.2	T2.0 ± 0.3	−0.05 ± 0.09	0.13 ± 0.10	0.28 ± 0.09	−0.02 ± 0.10	0.20 ± 0.10	...
L06-bright	1632+4150	T1.0	T1.0	1122−3512	T2.0	T2.0	−0.16	0.02	0.17	−0.14	0.08	13.7
	⟨Primary⟩	T1.0 ± 0.2	T1.0 ± 0.2	⟨Secondary⟩	T2.0 ± 0.4	T2.0 ± 0.4	−0.13 ± 0.14	0.06 ± 0.20	0.21 ± 0.19	−0.10 ± 0.15	0.13 ± 0.23	...
L06-bright (IC)	1632+4150	T1.0	T1.0	1122−3512	T2.0	T2.0	−0.15	0.03	0.18	−0.13	0.09	13.7
	⟨Primary⟩	T1.0 ± 0.2	T1.0 ± 0.2	⟨Secondary⟩	T2.0 ± 0.3	T2.0 ± 0.4	−0.10 ± 0.12	0.08 ± 0.14	0.23 ± 0.13	−0.08 ± 0.13	0.15 ± 0.16	...
SDSS J120602.51+281328.7												
Single	1750+1759	T3.5	T3.0	...	...	...	...	...	...	...	...	27.3
L06-faint	1122−3512	T2.0	T2.0	1901+4718	T5.0	T5.0	0.23	0.84	0.98	0.31	1.05	22.8
	⟨Primary⟩	T2.0 ± 0.2	T2.0 ± 0.2	⟨Secondary⟩	T4.5 ± 0.4	T4.5 ± 0.3	0.16 ± 0.10	0.73 ± 0.19	0.86 ± 0.18	0.24 ± 0.11	0.93 ± 0.22	...
L06-faint (IC)	1122−3512	T2.0	T2.0	1901+4718	T5.0	T5.0	0.14	0.75	0.88	0.21	0.96	23.2
	⟨Primary⟩	T2.0 ± 0.3	T2.0 ± 0.3	⟨Secondary⟩	T4.5 ± 0.5	T4.5 ± 0.5	0.08 ± 0.14	0.62 ± 0.27	0.75 ± 0.26	0.16 ± 0.16	0.81 ± 0.32	...
L06-bright	1122−3512	T2.0	T2.0	0742+2055	T5.0	T5.0	0.49	1.17	1.37	0.61	1.44	26.7
	⟨Primary⟩	T2.0 ± 0.3	T2.0 ± 0.3	⟨Secondary⟩	T5.0 ± 0.5	T5.0 ± 0.6	0.42 ± 0.19	1.03 ± 0.34	1.20 ± 0.39	0.52 ± 0.22	1.26 ± 0.40	...
L06-bright (IC)	1122−3512	T2.0	T2.0	1901+4718	T5.0	T5.0	0.48	1.10	1.23	0.56	1.31	25.7
	⟨Primary⟩	T2.0 ± 0.4	T2.5 ± 0.4	⟨Secondary⟩	T4.5 ± 0.6	T4.5 ± 0.7	0.37 ± 0.33	0.91 ± 0.52	1.06 ± 0.51	0.45 ± 0.37	1.11 ± 0.59	...
SDSS J120747.17+024424.8												
Single	0151+1244	T1.0	T0.0	...	...	...	...	...	...	...	...	44.6
L06-faint	1036−3441	L6.0	L6.5	1209−1004	T3.0	T3.0	0.74	1.24	1.77	0.87	1.38	6.14
	⟨Primary⟩	L6.5 ± 0.7	L6.5 ± 0.4	⟨Secondary⟩	T2.5 ± 0.5	T2.5 ± 0.5	0.48 ± 0.28	0.90 ± 0.31	1.45 ± 0.28	0.62 ± 0.30	1.01 ± 0.31	...
L06-faint (IC)	1036−3441	L6.0	L6.5	1048+0919	T2.5	T2.5	0.47	0.87	1.36	0.59	0.97	4.95
	⟨Primary⟩	L6.0 ± 0.5	L7.0 ± 0.2	⟨Secondary⟩	T2.5 ± 0.3	T2.0 ± 0.2	0.43 ± 0.13	0.83 ± 0.12	1.32 ± 0.06	0.55 ± 0.13	0.92 ± 0.11	...
L06-bright	1515+4847	L6.0	L5.5	1254−0122	T2.0	T2.0	0.11	0.34	0.68	0.26	0.37	4.38
	⟨Primary⟩	L5.5 ± 0.4	L5.5 ± 0.2	⟨Secondary⟩	T2.0 ± 0.2	T2.0 ± 0.2	0.20 ± 0.16	0.43 ± 0.15	0.76 ± 0.14	0.36 ± 0.17	0.46 ± 0.15	...
L06-bright (IC)	1515+4847	L6.0	L5.5	1254−0122	T2.0	T2.0	0.24	0.47	0.82	0.40	0.51	4.18
	⟨Primary⟩	L6.0 ± 0.3	L5.5 ± 0.2	⟨Secondary⟩	T2.0 ± 0.2	T2.0 ± 0.2	0.24 ± 0.01	0.47 ± 0.02	0.81 ± 0.02	0.40 ± 0.00	0.50 ± 0.02	...
SDSS J151643.01+305344.4												
Single	1007+1930	L8.0	L9.5	...	...	...	...	...	...	...	...	8.38
L06-faint	1043+2225	L8.0	L9.0	0830+4828	L9.0	L9.5	0.05	0.13	0.24	0.07	0.16	7.28
	⟨Primary⟩	L8.0 ± 0.2	L9.0 ± 0.5	⟨Secondary⟩	L9.5 ± 1.2	T0.0 ± 0.9	0.06 ± 0.24	0.21 ± 0.33	0.34 ± 0.39	0.08 ± 0.25	0.25 ± 0.42	...
L06-faint (IC)	1043+2225	L8.0	L9.0	0830+4828	L9.0	L9.5	−0.10	−0.02	0.09	−0.08	0.00	7.22
	⟨Primary⟩	L8.0 ± 0.2	L9.0 ± 0.6	⟨Secondary⟩	L9.5 ± 0.9	T0.0 ± 0.8	−0.09 ± 0.13	0.05 ± 0.23	0.19 ± 0.35	−0.07 ± 0.16	0.08 ± 0.27	...

Table 9
(Continued)

Mode[b] (1)	Primary (2)	Pub SpT (3)	SpeX SpT (4)	Secondary (5)	Pub SpT (6)	SpeX SpT (7)	ΔJ (8)	ΔH (9)	ΔK (10)	$\Delta F110W$ (11)	$\Delta F170M$ (12)	χ^2 (13)
L06-bright	1043+2225	L8.0	L9.0	0830+4828	L9.0	L9.5	−0.14	−0.06	0.06	−0.11	−0.03	7.20
	⟨Primary⟩	L8.0 ± 0.2	L9.0 ± 0.5	⟨Secondary⟩	T0.0 ± 2.8	T0.5 ± 2.6	−0.01 ± 0.55	0.29 ± 0.97	0.50 ± 1.18	0.04 ± 0.63	0.42 ± 1.25	...
L06-bright (IC)	1043+2225	L8.0	L9.0	0830+4828	L9.0	L9.5	−0.18	−0.10	0.02	−0.15	−0.07	7.19
	⟨Primary⟩	L8.0 ± 0.2	L9.0 ± 0.5	⟨Secondary⟩	T0.0 ± 2.7	T0.5 ± 2.6	−0.06 ± 0.51	0.24 ± 0.94	0.46 ± 1.17	−0.01 ± 0.60	0.37 ± 1.22	...
SDSS J205235.31-160929.8												
Single	0151+1244	T1.0	T0.0	...	...	...	...	...	...	...	...	6.23
L06-faint	1155+0559	L7.5	L7.0	1122−3512	T2.0	T2.0	−0.01	0.40	1.07	0.11	0.53	2.59
	⟨Primary⟩	L7.5 ± 0.6	L7.0 ± 0.5	⟨Secondary⟩	T2.0 ± 0.2	T2.0 ± 0.2	0.04 ± 0.18	0.45 ± 0.18	1.10 ± 0.17	0.16 ± 0.18	0.58 ± 0.18	...
L06-faint (IC)	2047−0718	T0.0	L7.5	1048+0919	T2.5	T2.5	0.29	0.70	1.13	0.41	0.78	2.19
	⟨Primary⟩	L9.5 ± 1.3	L7.5 ± 0.3	⟨Secondary⟩	T2.5 ± 0.3	T2.0 ± 0.2	0.29 ± 0.06	0.70 ± 0.06	1.13 ± 0.07	0.41 ± 0.05	0.77 ± 0.05	...
L06-bright	1036−3441	L6.0	L6.5	0136+0933	T2.5	T2.0	−0.01	0.39	0.81	0.11	0.46	2.94
	⟨Primary⟩	L6.0 ± 0.6	L6.5 ± 0.4	⟨Secondary⟩	T2.5 ± 0.2	T2.0 ± 0.2	−0.08 ± 0.16	0.32 ± 0.15	0.78 ± 0.13	0.05 ± 0.16	0.40 ± 0.15	...
L06-bright (IC)	1526+2043	L7.0	L5.5	1048+0919	T2.5	T2.5	−0.10	0.29	0.85	0.06	0.40	3.30
	⟨Primary⟩	L7.0 ± 1.2	L6.5 ± 0.9	⟨Secondary⟩	T2.0 ± 0.5	T2.0 ± 0.5	−0.17 ± 0.26	0.18 ± 0.24	0.69 ± 0.25	−0.02 ± 0.28	0.27 ± 0.24	...

Notes.

[a] For each source, we list the parameters of the best-fitting template (minimum χ^2) for each of the fitting modes; for the composite fits, we also give mean parameters for the primary (⟨Primary⟩) and secondary (⟨Secondary⟩), as well as the predicted relative magnitudes in the MKO *JHK* and *HST*/NICMOS $F110W$ and $F170M$ bands.

[b] Spectral fitting mode: Single: fits to single templates; L06-faint and L06-bright: fits to composite templates using the Liu et al. (2006) faint and bright M_K/spectral type relations, respectively; L06-faint (IC) and L06-bright (IC): fits to composite templates using the Liu et al. (2006) faint and bright relations, respectively, and the index-based spectral classifications.

J0351+4810 satisfied all six selection criteria, and the best-fit composite is a clear improvement over the best-fit single template and statistically significant. Average primary and secondary spectral types are L6.5 ± 0.7 and T5 ± 0.7, with a secondary that may be slightly brighter than the primary at the 1.05 μm and 1.27 μm spectral flux peaks ($\Delta J = 0.31 \pm 0.31$). The primary in the best-fit composite, 2MASS J0103+1935 (L6, 2MASS $J - K_s = 2.14 \pm 0.10$), has a fairly steep red spectral slope, indicative of either low surface gravity (i.e., youth) or unusually thick condensate clouds (e.g., Looper et al. 2008b). On the other hand, the best-fit secondary has a normal color for its spectral type. This combination suggests a system with an unusually cloudy primary and normal secondary. No high angular resolution imaging observations of SDSS J0351+4810 have been reported to date.

5.1.3. SDSS J103931.35+325625.5

Chiu et al. (2006) classified SDSS J1039+3256 a T1 in the near-infrared (our SpeX classification is T1.5), and its spectrum satisfied all six selection criteria. The best-fit composite is a clear improvement over the best-fit single template and statistically significant. Average primary and secondary spectral types are L7 ± 0.2 and T4 ± 0.2, and the primary appears to be brighter than the secondary at all wavelengths ($\Delta J = 0.26 \pm 0.09$). The components of the best-fit composite appear to be fairly normal for their respective spectral types. No high angular resolution imaging observations of SDSS J1039+3256 have been reported to date.

5.1.4. 2MASS J11061197+2754225

Looper et al. (2007) classified 2MASS J1106+2754 a T2.5 in the near-infrared; we classified the same SpeX spectrum T2 using spectral indices. Satisfying three selection criteria, 2MASS J1106+2754 is subtly but significantly better fit by composites with average component types of T0 ± 0.2 and T4.5 ± 0.2. These types are similar to those inferred for 2MASS J1404+3159, and predict a secondary that is substantially brighter at the 1.05 μm and 1.27 μm spectral flux peaks ($\Delta J = -0.37 \pm 0.06$). Again, the best-fit primary is SDSS J1520+3546, a somewhat peculiar blue late-L/early-T dwarf.

2MASS J1106+2754 is one of the only two strong candidates imaged at high angular resolution, in this case by Looper et al. (2008a) using the Keck AO system. K_s-band images show only a single point source with a point spread function full width at half-maximum of 68 mas. Based on the relative magnitudes inferred from this analysis ($\Delta K = 1.16 \pm 0.09$ for the faint calibration), this observation rules out a resolved binary system with projected separation $\gtrsim$1.5 AU at the time of the observation, assuming a distance of 22 pc (Looper et al. 2007). The null imaging result indicates one of the three possibilities: 2MASS J1106+2754 may be a single source, a binary observed close to line-of-sight alignment (e.g., Kelu-1; Martín et al. 1999a; Liu & Leggett 2005; Gelino et al. 2006), or a tightly separated system. The excellent fit of this source's spectrum to composites supports one of the two latter possibilities, and 1.5 AU is not a particularly stringent constraint on the separation given that several brown dwarf multiple systems are known to have even smaller separations (e.g., Basri & Martín 1999; Stassun et al. 2006; Joergens & Müller 2007). Nevertheless, second-epoch imaging and/or spectroscopic monitoring are required to verify the binary nature of this source.

5.1.5. 2MASS J13243559+6358284

Discovered independently by Looper et al. (2007) and Metchev et al. (2008), 2MASS J1324+6358 was classified as a peculiar T2 in the former study based on its unusually red near-infrared spectral energy distribution (our SpeX classification is T2 ± 1). 2MASS J1324+6358 is also a red outlier in optical, near-infrared, and mid-infrared colors (Looper et al. 2007; Metchev et al. 2008; Faherty et al. 2009). Looper et al. specifically examined the possibility that this source is an unresolved binary, finding a good match to an L9 + T2 composite. We also find this source to be a likely binary, with statistically significant better fits to composites with mean component types of L8 ± 0.2 and T3.5 ± 0.2. The secondary of this system appears to be brighter than the primary at the 1.05 μm and 1.27 μm

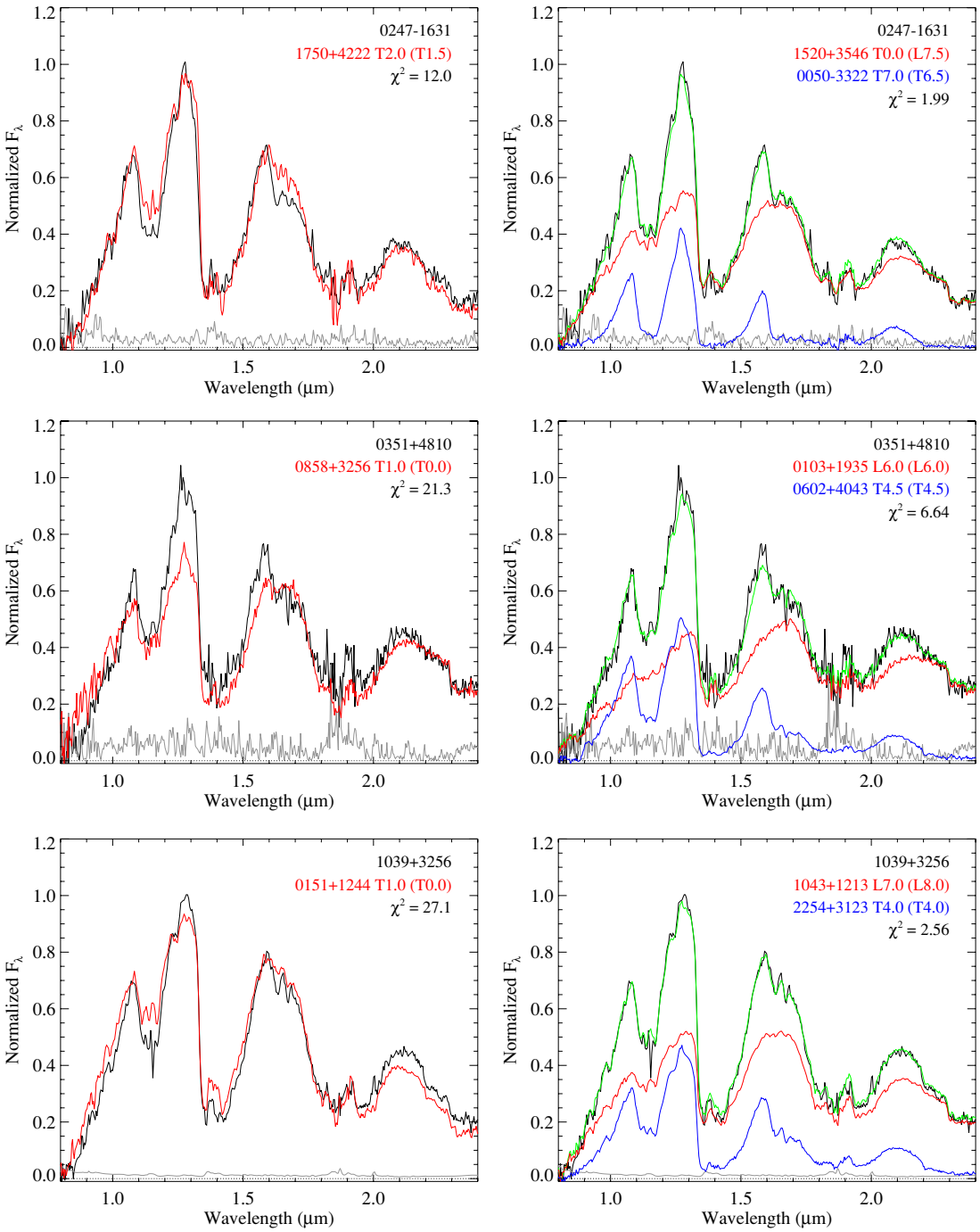

Figure 6. Spectral fits to the sources identified as "strong" binary candidates (at least three selection criteria satisfied). For each row, the left panel shows the best-fit single template (red lines) compared to the source spectrum (black lines, noise spectrum in gray), while the right panel shows the best-fit composite (green lines), primary (red lines), and secondary spectra (blue lines). Source spectra are normalized to the peak flux in the 1.0–1.3 μm range, while single and composites are normalized to minimize χ^2 deviations. Component spectra in the right panels are normalized to their respective contribution to the composite, according to the faint Liu et al. (2006) relation (see Section 4.1). Template source names, literature and index-based spectral types (the latter in parentheses) and the corresponding χ^2 deviations are labeled in the top right corner of each panel.

(A color version of this figure is available in the online journal.)

flux peaks ($\Delta J = -0.05 \pm 0.06$). The primary component of the best-fit composite, 2MASS J1043+2225 (2MASS $J - K_s = 1.97 \pm 0.08$), has been noted as one of the reddest optically classified L8 dwarfs known (Cruz et al. 2007), while the secondary has normal colors for its spectral type. Like SDSS J0351+4810, this combination suggests a system with an unusually cloudy primary and cloud-free T dwarf secondary. No high angular resolution imaging observations of 2MASS J1324+6358 have been reported to date.

5.1.6. SDSS J141530.05+572428.7

Chiu et al. (2006) classified SDSS J1415+5724 a T3 $\pm$ 1 (same as our SpeX classification), with an uncertainty driven

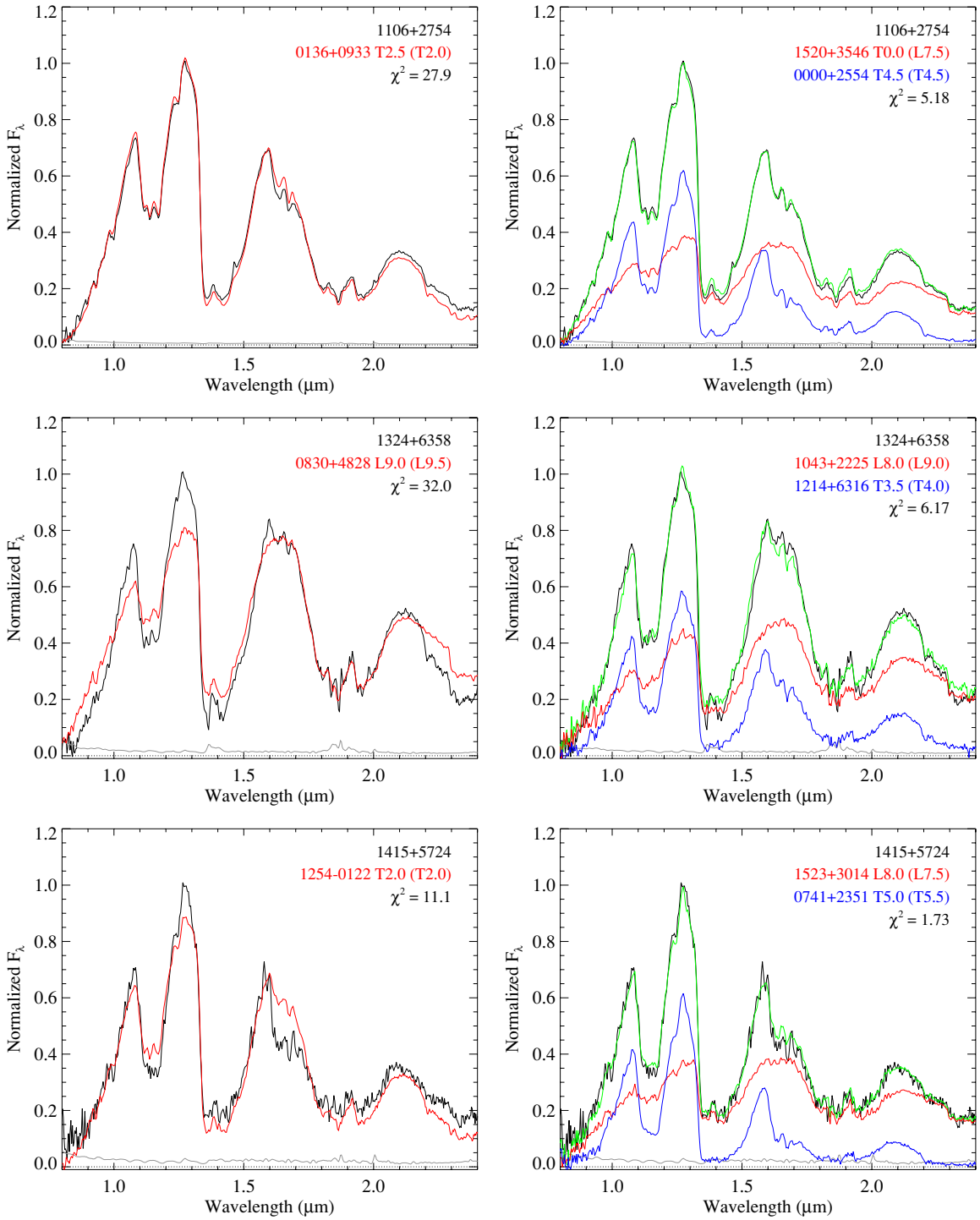

Figure 6. (Continued)

by weak 2.2 μm CH_4 absorption relative to the pronounced 1.6 μm band. Both Chiu et al. (2006) and Faherty et al. (2009) note this source as being unusually red for its spectral type, and the former attempted (unsuccessfully) to reproduce its spectrum as a binary. SDSS J1415+5724 satisfied all six selection criteria, and composites (average types L8 $\pm$ 0.5 and T5 $\pm$ 0.3) provide visually obvious and statistically significant better fits to its spectrum. The secondary component appears to be brighter than the primary at the 1.05 μm and 1.27 μm spectral peaks ($\Delta J = -0.13 \pm 0.20$), and both components in the best-fit composite have normal colors and spectral energy distributions for their respective spectral types. No high angular resolution imaging observations of SDSS J1415+5724 have been reported to date.

5.1.7. SDSS J143553.25+112948.6

Chiu et al. (2006) classified SDSS J1435+1129 a T2 $\pm$ 1 in the near-infrared (consistent with our T2.5 $\pm$ 1 SpeX classification), with the uncertainty driven by weak 2.2 μm CH_4 absorption relative to 1.1 μm and 1.6 μm bands. Its spectrum satisfied all six selection criteria, and the best-fit composite

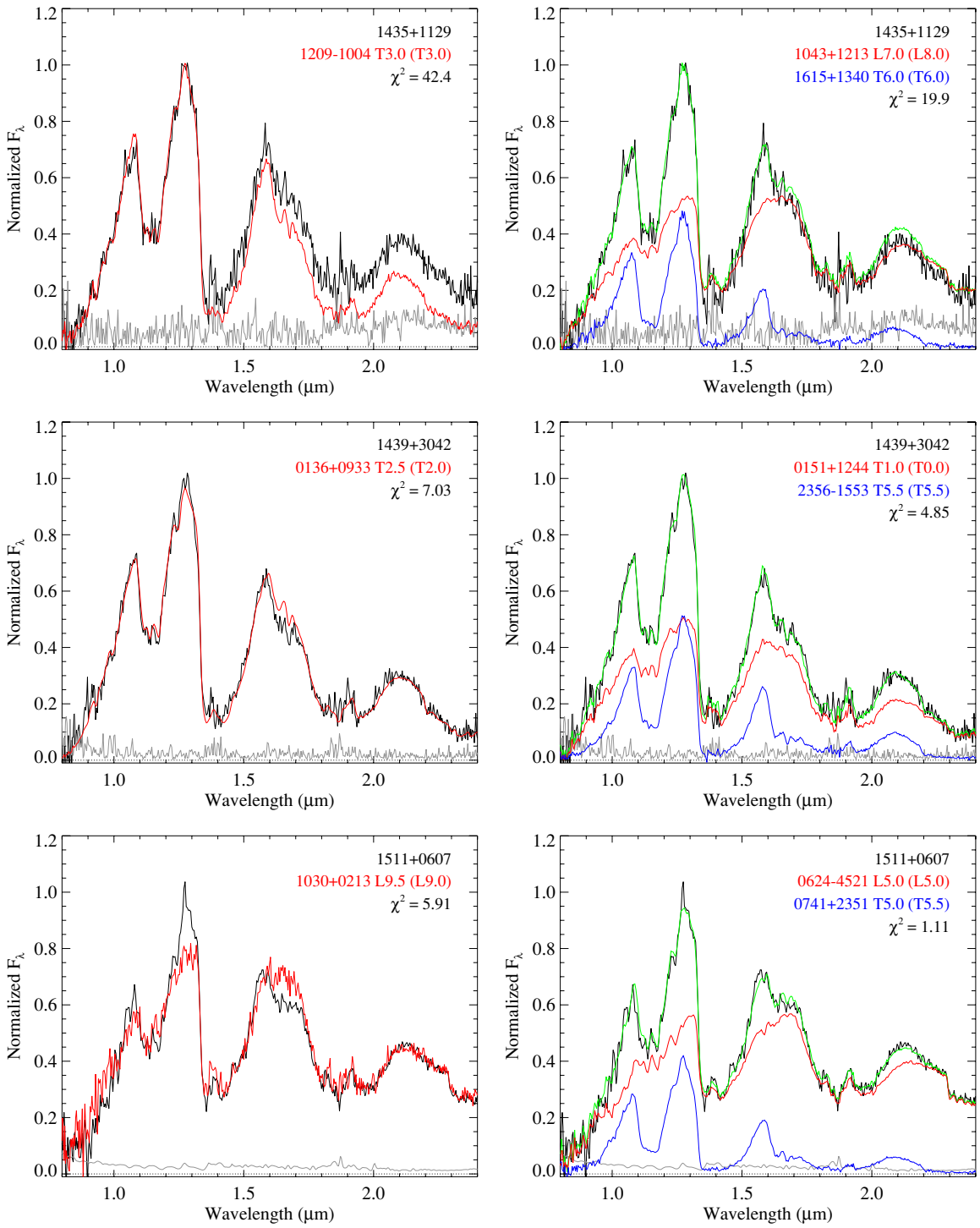

Figure 6. (Continued)

is a visually better match than the best-fit single template, reproducing in particular the broad *K*-band peak and relatively strong 1.6 μm CH_4 absorption. The average component types, L7.5 $\pm$ 0.4 and T6 $\pm$ 0.3, indicate a secondary that is slightly fainter than the primary throughout the near-infrared (ΔJ = 0.41 $\pm$ 0.12). The components of the best-fitting composite appear to have normal colors and spectral energy distributions for their respective spectral types. No high angular resolution imaging observations of SDSS J1435+1129 have been reported to date.

5.1.8. SDSS J143945.86+304220.6

Chiu et al. (2006) classified SDSS J1439+3042 a T2.5, identical to our index-based classification. Its spectrum satisfied only four selection criteria, but the best-fit composite is a statistically significantly (albeit subtle) better match than the best-fit single template, providing a better fit to the strong 1.6 μm CH_4 band and blueshifted *K*-band peak. Average component types of T1 $\pm$ 0.2 and T5 $\pm$ 0.6 indicate a secondary component that may be slightly brighter than the primary at the 1.27 μm spectral flux

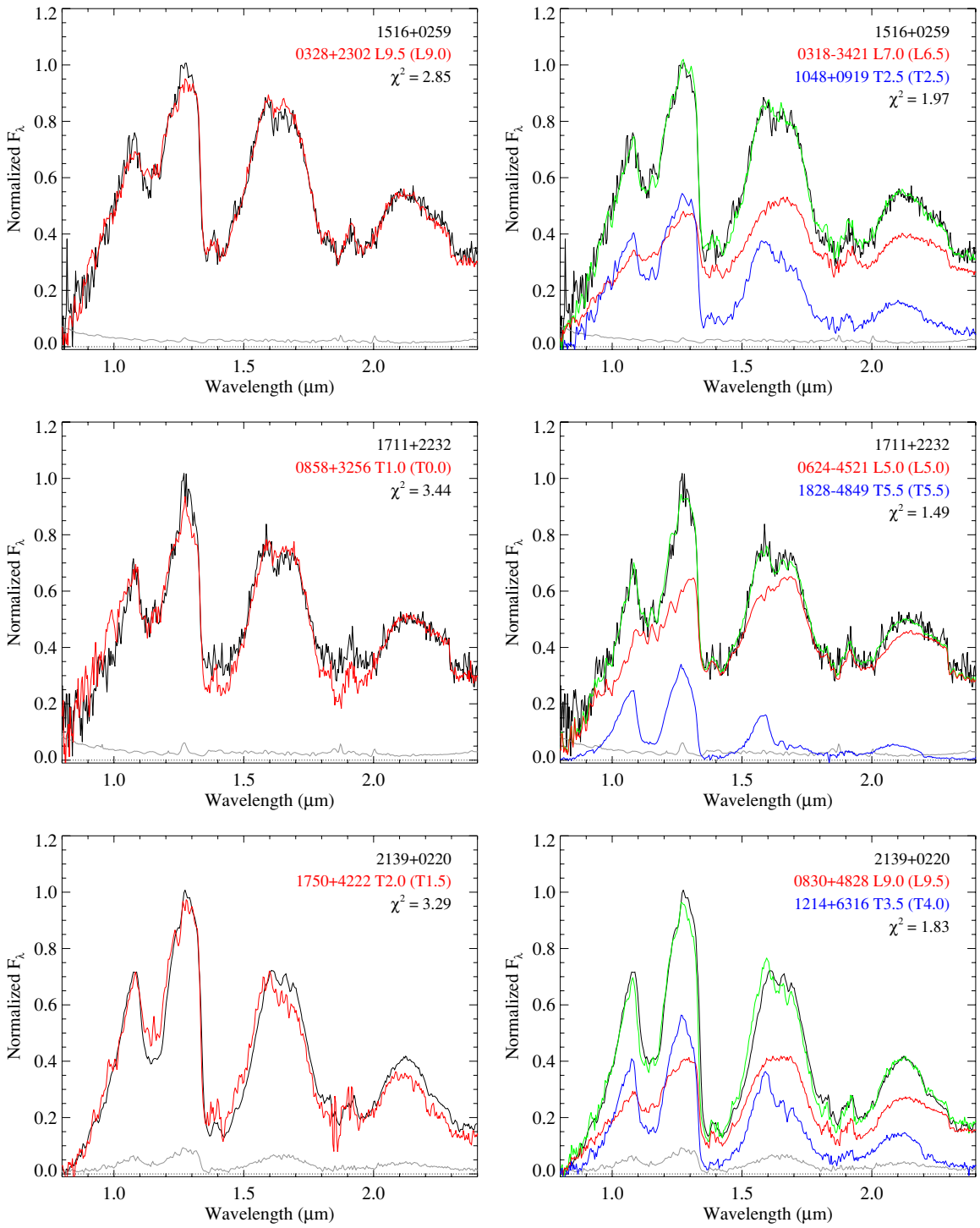

Figure 6. (Continued)

peak ($\Delta J = 0.06 \pm 0.24$). The best-fit binary components have normal colors and spectral energy distributions for their respective types. No high angular resolution imaging observations of SDSS J1439+3042 have been reported to date.

5.1.9. SDSS J151114.66+060742.9

Chiu et al. (2006) classified SDSS J1511+0607 a T0 ± 2 in the near-infrared (our SpeX type is T0.5 ± 2), with the large uncertainty arising from substantial scatter in index subtypes (L7–T2) on the Geballe et al. (2002) scheme. Its spectrum is clearly peculiar, with strong CH_4 absorption at 1.1 μm and 1.6 μm, but very weak absorption at 2.2 μm; these features are similar in nature to the resolved binary 2MASS J0518-2828. The spectrum of SDSS J1511+0607 satisfied all six selection criteria, and the best-fit composite is a visually obvious and statistically significant better match than the best-fit single template. Average component types, L5.5 ± 0.8 and T5 ± 0.4, indicate a secondary component that is fainter than the primary across the near-infrared band ($\Delta J = 0.54 \pm 0.32$). The primary component of the best-fit composite, SDSS J0624-4521 (L5, 2MASS $J - K_s = 1.88 \pm 0.04$) is somewhat red for its spectral type, while the secondary has normal colors. Hence, this may be another system

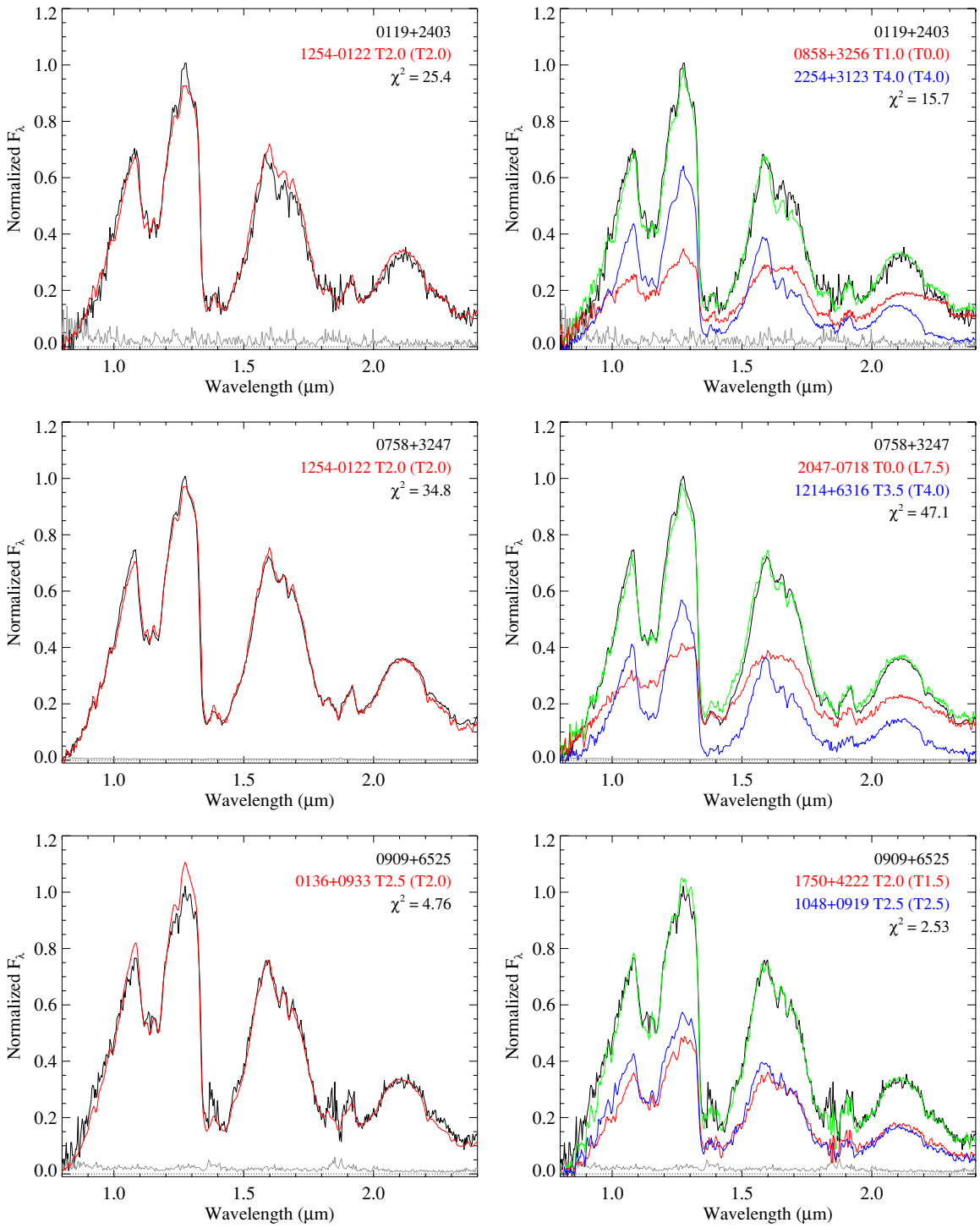

Figure 7. Same as Figure 6 but for "weak" binary candidates (satisfying only two selection criteria).
(A color version of this figure is available in the online journal.)

with an unusually cloudy primary but normal secondary. No high angular resolution imaging observations of SDSS J1511+0607 have been reported to date.

5.1.10. SDSS J151603.03+025928.9

Knapp et al. (2004) classified SDSS J1516+0259 a T0 ± 1.5 on the near-infrared scheme of Geballe et al. (2002); our SpeX classification is L9.5 ± 1. The uncertainties in both arise from weak CH_4 absorption at 2.2 μm compared to the 1.1 μm and 1.6 μm bands. The spectrum of this source satisfied four of the spectral index criteria, and the best-fit composite is a significantly better match than the best-fit single template, 2MASS J0328+2302, which may itself be a unresolved binary (see Section 6.1). The average component types inferred for SDSS J1516+0259, L7.5 ± 1.1 and T2.5 ± 2.2, are rather poorly constrained, as are the relative brightnesses ($\Delta J = 0.30 \pm 0.65$). Notably, the best-fit composite combines a somewhat red L7 (2MASS J0318−3421, 2MASS $J - K_s = 2.06 \pm 0.07$) and a fairly normal T2.5, again suggesting a system with a cloudy

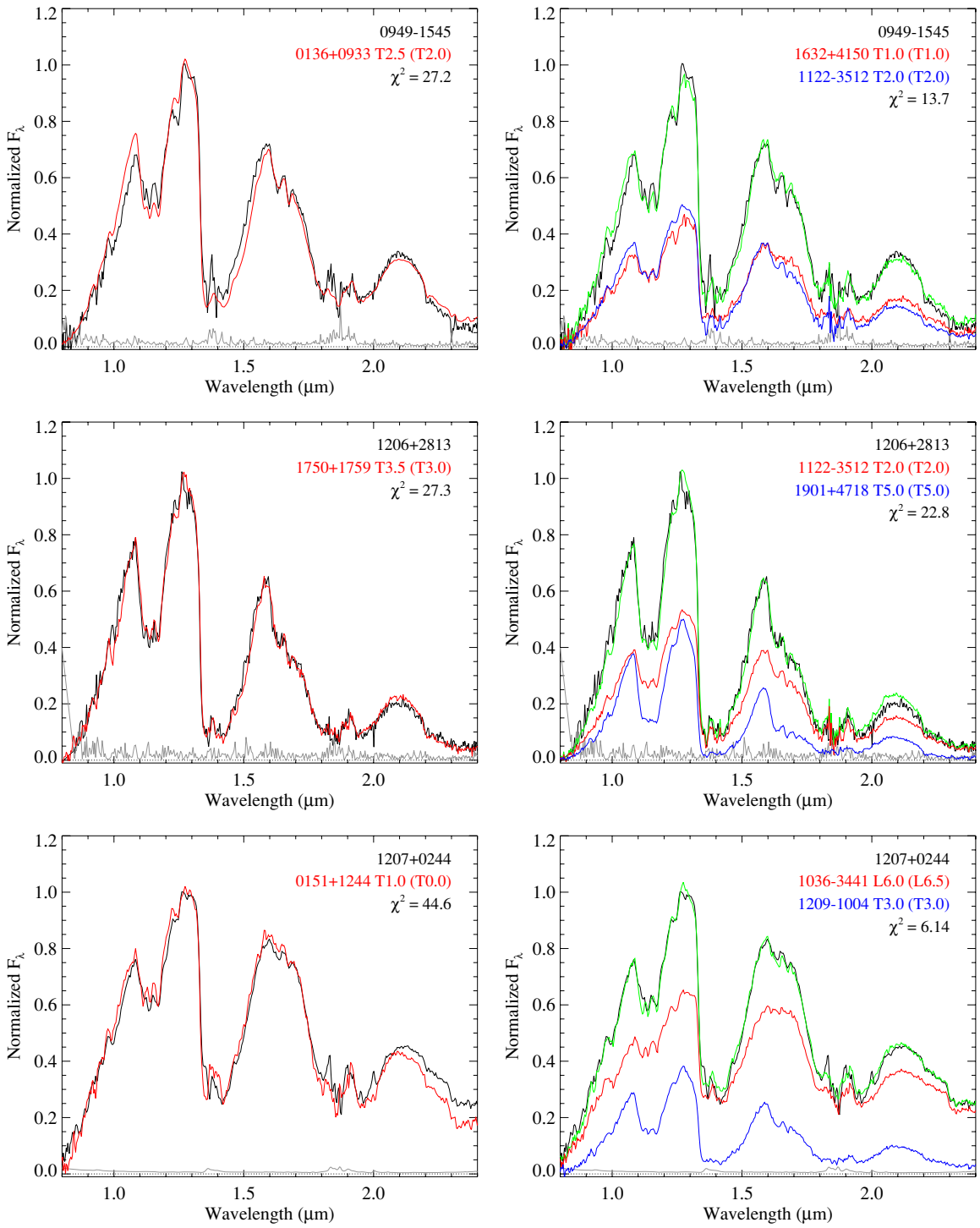

Figure 7. (Continued)

primary but normal secondary. No high angular resolution imaging observations of SDSS J1516+0259 have been reported to date.

5.1.11. 2MASS J1711457+223204

2MASS J1711+2232 has been studied extensively in the literature, originally identified in the 2MASS survey and classified L6.5 in the optical with no detectable lithium absorption or Hα emission (Kirkpatrick et al. 2000). We derive a later but poorly constrained near-infrared classification of L9 $\pm$ 3 based on strong H_2O absorption and an indication of weak CH_4 absorption at 1.6 μm. 2MASS J1711+2232 was also examined in the near-infrared by Nakajima et al. (2004), who noted the presence of CH_4 at 2.2 μm but not at 1.6 μm; our SpeX spectrum in fact shows the opposite, although the *K*-band data have a somewhat lower signal-to-noise ratio. Tsuji et al. (2004) commented on the unusual 1.6 μm spectral morphology of this source, suggesting that it may be due to absorption from FeH and possibly some other unidentified species.

That other species is likely to be CH_4 from an unresolved T dwarf companion, as the unusual feature at 1.6 μm seen in the SpeX spectrum of 2MASS J1711+2232 (which satisfied all

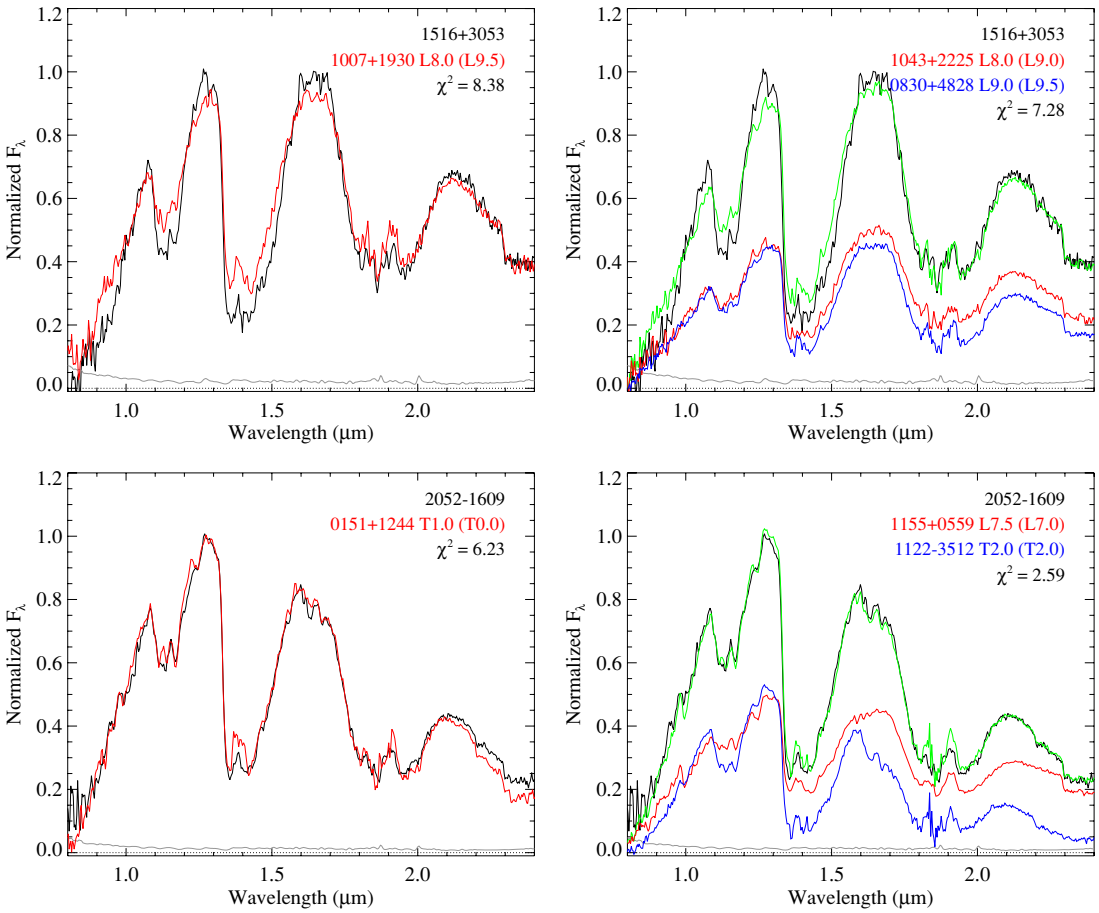

Figure 7. (Continued)

six selection criteria) is similar to those noted in the spectra of 2MASS J0320−0446, SDSS J0805+4812, and Kelu-1A. The best-fit composite is a significantly better match than our best-fit single template, reproducing the 1.6 μm feature in detail. Mean component types of L5 $\pm$ 0.4 and T5.5 $\pm$ 1.2 are similar to those inferred for SDSS J0805+4812 (L4.5 $\pm$ 0.7 and T5 $\pm$ 0.6; Burgasser 2007b). The secondary is considerably fainter than the primary across the near-infrared ($\Delta J = 0.92 \pm 0.32$, $\Delta K = 3.05 \pm 0.60$).

2MASS J1711+2232 has been imaged at high angular resolution with *HST*/WFPC2 (Gizis et al. 2003) and reported to be unresolved in both F814W ($\lambda_c = 0.79\,\mu$m) and F1042M ($\lambda_c = 1.02\,\mu$m) bands. However, the sensitivity of these observations were insufficient to detect the T dwarf component; the primary/combined source was marginally detected at F1042M, where the much fainter secondary (ΔF1042M $\approx$ 2–3) would have been brightest. Hence, in the absence of sufficiently sensitive near-infrared *HST* or AO observations, we cannot determine conclusively whether this system is a tight (unresolvable) binary. 2MASS J1711+2232 is the only binary candidate in our sample with a parallactic distance measurement ($d = 30 \pm 4$ pc; Vrba et al. 2004). Its component absolute magnitudes are discussed further in Section 6.1.

5.1.12. 2MASS J21392676+0220226

2MASS J2139+0220 was classified T0 by Reid et al. (2008) based on its red optical spectrum, and T1.5 in the near-infrared by Burgasser et al. (2006b) based on the SpeX spectrum examined here (indices yield a T2.5 $\pm$ 1 spectral type). Its near-infrared color is somewhat red for its spectral type: 2MASS $J - K_s = 1.68 \pm 0.07$ as compared to $\langle J - K_s \rangle = 1.31$ for T1 dwarfs and $\langle J - K_s \rangle = 1.02$ for T2 dwarfs (Faherty et al. 2009). The spectrum of 2MASS J2139+0220 satisfied only three selection criteria, but this source nevertheless appears to be a strong binary candidate as its best-fit composite is a significant improvement over the best-fit single template. However, the fit is not perfect, failing to reproduce the weak 1.6 μm CH_4 band relative to strong 1.1 μm and 2.2 μm absorptions. The inferred average component types, L8.5 $\pm$ 0.7 and T3.5 $\pm$ 1.0, are also somewhat poorly constrained. Given its unusual pattern of CH_4 features even for an unresolved binary, the components of 2MASS J2139+0220 may themselves have unusual properties. Its best-fitting primary, the L9 $\pm$ 1 SDSS J0830+4828, has a large tangential velocity ($V_{\rm tan} = 79 \pm 4$ km s^{-1}; Faherty et al. 2009) although its absolute brightness and infrared colors appear to be normal (Geballe et al. 2002; Vrba et al. 2004; Leggett et al. 2007). The inferred composition of this system indicates a secondary that is substantially brighter than the primary at the 1.05 μm and 1.27 μm spectral peaks ($\Delta J = -0.14 \pm 0.21$). No high angular resolution imaging observations of 2MASS J2139+0220 have been reported to date.

5.2. Weak Candidates

5.2.1. SDSS J011912.22+240331.6

Chiu et al. (2006) classified SDSS J0119+2403 a T2 in the near-infrared (similar to our index-based T2.5 classification),

and its spectrum exhibits a slightly enhanced *J*-band peak and stronger 1.6 μm CH_4 absorption relative to the T2 spectral standard, SDSS J1254−0122. The best-fit composite is a subtle but significant improvement over the best-fit single template, with inferred component types of T0 ± 0.7 and T4 ± 0.4, similar to those of the resolved binary 2MASS J1404–3159. Like that source, the secondary of SDSS J0119+2403 appears to be substantially brighter than the primary at the 1.05 μm, 1.27 μm, and possibly 1.6 μm spectral peaks ($\Delta J = -0.42 \pm 0.19$). The best-fit primary, SDSS J0858+3256 (T1, MKO $J-K = 1.61 \pm 0.04$) is noted to be a red outlier for its spectral type with a large tangential velocity ($V_{\rm tan} = 66 \pm 3$ km s^{-1}; Faherty et al. 2009), while the best-fit secondary is an unexceptional T4 dwarf. Hence, this system may again be composed of an unusually cloudy primary and cloud-free secondary. No high angular resolution imaging observations of SDSS J0119+2403 have been reported to date.

5.2.2. SDSS J075840.33+324723.4

Knapp et al. (2004) classified SDSS J0758+3247 a T2 ± 1 on the Geballe et al. (2002) scheme, with an uncertainty driven by strong H_2O/CH_4 absorption at 1.1 μm (our SpeX classification is T2.5). This source is in fact a near-clone to SDSS J1254-0122, and our binary templates actually provide significantly *worse* fits (higher χ^2 values) than this best-fit single template. While SDSS J1254-0122 also satisfied one of our binary selection criteria, it is unresolved in *HST* imaging observations (Burgasser et al. 2006c) so we cannot exclude the possibility that both sources are single brown dwarfs. No high angular resolution imaging observations of SDSS J0758+3247 have been reported to date.

5.2.3. SDSS J090900.73+652527.2

Chiu et al. (2006) classified SDSS J0909+6525 a T1.5 in the near-infrared, identical to our SpeX classification, and its spectrum is fairly similar to that of the bright T2.5 IPMS J0136+0933. The MKO $J - K = 0.62 \pm 0.04$ color of SDSS J0909+6525 is somewhat blue for its spectral type, and Faherty et al. (2009) specifically note it as a blue outlier with a normal tangential velocity ($V_{\rm tan} \approx 28$ km s^{-1}). The best-fit composite is a subtle but significantly better match to the spectrum of SDSS J0909+6525, indicating average component types of T1.5 ± 0.5 and T2.5 ± 0.3 and a secondary that is somewhat brighter than the primary at the 1.05 μm and 1.27 μm spectral peaks ($\Delta J = -0.12 \pm 0.10$). The best-fitting composite components have normal colors and spectral energy distributions for their respective spectral types. No high angular resolution imaging observations of SDSS J0909+6525 have been reported to date.

5.2.4. 2MASS J09490860−1545485

Tinney et al. (2005) classified 2MASS J0949−1545 a T1 ± 1 in the near-infrared (our SpeX classification is T1.5), the uncertainty arising from strong 1.6 μm CH_4 absorption but weak 1.1 μm H_2O/CH_4 absorption as compared to spectral standards. The spectrum of this source is also similar to that of IPMS J0136+0933, but the best-fit composite is a significantly better match with components similar to SDSS J0909+6525, T1 ± 0.2 and T2 ± 0.2. Again, the secondary is inferred to be somewhat brighter than the primary at the 1.05 μm and 1.27 μm spectral peaks ($\Delta J = -0.07 \pm 0.05$) despite having comparable spectral types. The best-fit composite components are normal for their respective classifications. No high angular resolution imaging observations of 2MASS J0949−1545 have been reported to date.

5.2.5. SDSS J120602.51+281328.7

Chiu et al. (2006) classified SDSS J1206+2813 a T3 in the near-infrared (identical to our SpeX classification), and it exhibits somewhat blue near-infrared colors for its spectral type, MKO $J-K = 0.13 \pm 0.04$ versus $\langle J - K \rangle = 0.56 \pm 0.22$ for other T2.5–T3.5 dwarfs (Chiu et al. 2006). Its spectrum is nearly identical to that of the T3.5 SDSS J1750+1759, and while our best-fit composite provides a slight reduction in χ^2, at 92% confidence it falls just short of our significance threshold. It is possible that SDSS J1206+2813 fails the binary significance criteria because SDSS J1750+1759 is itself an unresolved binary, as suggested by its apparent overluminosity compared to other early-type T dwarfs (Vrba et al. 2004; Liu et al. 2006). However, SDSS J1750+1759 was unresolved in *HST* images (Burgasser et al. 2006c) and it did not satisfy any of our spectral index selection criteria. Hence, we cannot rule out that both sources are single brown dwarfs. No high angular resolution images of SDSS J1206+2813 have been reported to date.

5.2.6. SDSS J120747.17+024424.8

Hawley et al. (2002) classified SDSS J1207+0244 an L8 based on red optical data, while Knapp et al. (2004) classified it T0 in the near-infrared (identical to our SpeX classification). The spectrum of SDSS 1207+0244 is very similar to that of the resolved binary SDSS J0423–0414, and as a consequence it was chosen to replace the latter as the T0 spectral standard in the classification scheme of Burgasser et al. (2006b). However, it appears that this source may also be a binary system, as the best-fit composite provides a significantly better match to its spectrum. The mean component types, L6.5 ± 0.7 and T2.5 ± 0.5 are similar to those inferred for SDSS J0423–0414 (Table 7), the secondary being fainter than the primary throughout the near-infrared ($\Delta J = 0.48 \pm 0.28$). The components of the best-fitting composite are normal, although the T3 2MASS J1209−1004 satisfied one of our selection criteria. The possibility that SDSS J1207+0244 is a binary system with very different component types is potentially problematic for the currently defined T dwarf classification scheme. High angular resolution images of this source have yet to be reported.

5.2.7. SDSS J151643.01+305344.4

Chiu et al. (2006) classified SDSS J1516+3053 a T0.5 ± 1 while our SpeX classification is T1.5 ± 2. The uncertainties in both arise from this source's unusually red spectral energy distribution and anomalously strong H_2O absorption bands. Leggett et al. (2007) also note this source as being unusually red in mid-infrared colors, and comparison to model colors suggest the presence of strong vertical mixing and thick condensate clouds in its atmosphere (Ackerman & Marley 2001; Saumon & Marley 2008). Chiu et al. (2006) attempted to fit their spectral data to a binary model, but did not find an adequate match. Our analysis concurs with that result, as the best-fit composite is only a marginal improvement over the best-fit single template (87% confidence level), and notably fails to reproduce the strong H_2O/CH_4 absorption feature at 1.1 μm. We therefore cannot rule out the possibility that this source is a single brown dwarf with unusual atmospheric properties. No high angular resolution imaging observations of SDSS J1516+3053 have been reported to date.

Table 10
Summary of Binary Candidates

Source	Spectral Types				ΔJ	CL[a]	AO/	Notes
	Pub	SpeX	Primary	Secondary			*HST*?	
(1)	(2)	(3)	(4)	(5)	(6)	(7)	(8)	(9)
Probable Binaries								
SDSS J011912.22+240331.6	T2	T2.5	T0.0 ± 0.7	T4.0 ± 0.4	−0.42 ± 0.19	>99%	No	Large *J* flux reversal Cloudy primary?
SDSS J024749.90−163112.6	T2 ± 1.5	T2.5 ± 1	T0.0 ± 0.2	T7.0 ± 0.3	0.68 ± 0.10	>99%	No	Old/metal-poor?
SDSS J035104.37+481046.8	T1 ± 1.5	T1.5 ± 1	L6.5 ± 0.7	T5.0 ± 0.7	0.31 ± 0.31	>99%	No	Small *J* flux reversal Cloudy primary?
SDSS J090900.73+652527.2	T1.5	T1.5	T1.5 ± 0.5	T2.5 ± 0.3	−0.12 ± 0.10	>99%	No	Small *J* flux reversal
2MASS J09490860−1545485	T2	T1.5 ± 1	T1.0 ± 0.2	T2.0 ± 0.2	−0.07 ± 0.05	>99%	No	Small *J* flux reversal
SDSS J103931.35+325625.5	T1	T1.5	L7.0 ± 0.2	T4.0 ± 0.2	0.26 ± 0.09	>99%	No	
2MASS J11061197+2754225	T2.5	T2.0	T0.0 ± 0.2	T4.5 ± 0.2	−0.37 ± 0.06	>99%	Yes	Large *J* flux reversal Old/metal-poor?
SDSS J120747.17+024424.8	T0	T0.0	L6.5 ± 0.7	T2.5 ± 0.5	0.48 ± 0.28	>99%	No	
2MASS J13243559+6358284	T2p	T2.0 ± 1	L8.0 ± 0.2	T3.5 ± 0.2	−0.05 ± 0.06	>99%	No	Large *J* flux reversal Cloudy primary?
SDSS J141530.05+572428.7	T3 ± 1	T3.0 ± 1	L8.0 ± 0.5	T5.0 ± 0.3	−0.18 ± 0.12	>99%	No	Large *J* flux reversal
SDSS J143553.25+112948.6	T2 ± 1	T2.5 ± 1	L7.5 ± 0.4	T6.0 ± 0.3	0.41 ± 0.12	>99%	No	
SDSS J143945.86+304220.6	T2.5	T2.5	T1.0 ± 0.2	T5.0 ± 0.6	0.10 ± 0.17	>99%	No	
SDSS J151114.66+060742.9	T0 ± 2	T0.5 ± 2	L5.5 ± 0.8	T5.0 ± 0.4	0.55 ± 0.26	>99%	No	Cloudy primary?
SDSS J151603.03+025928.9	T0:	L9.5 ± 1	L7.5 ± 1.1	T2.5 ± 2.2	0.30 ± 0.65	>99%	No	Small *J* flux reversal Cloudy primary?
2MASSI J1711457+223204	L6.5	L9.0 ± 3	L5.0 ± 0.4	T5.5 ± 1.2	0.92 ± 0.30	>99%	No[b]	π measurement
SDSS J205235.31−160929.8	T1 ± 1	T0.0 ± 1	L7.5 ± 0.6	T2.0 ± 0.2	0.04 ± 0.18	>99%	No	Small *J* flux reversal
2MASS J21392676+0220226	T1.5	T2.0 ± 1	L8.5 ± 0.7	T3.5 ± 1.0	−0.14 ± 0.21	>99%	No	Large *J* flux reversal
Other Sources								
SDSS J075840.33+324723.4	T2	T2.5	T0.0 ± 0.8	T3.5 ± 0.8	−0.31 ± 0.25	1%	No	Clone of SDSS J1254−0122
SDSS J120602.51+281328.7	T3	T3.0	T2.0 ± 0.2	T4.5 ± 0.4	0.16 ± 0.10	92%	No	Clone of SDSS J1750+1759
SDSS J151643.01+305344.4	T0.5 ± 1	T1.5 ± 2	L8.0 ± 0.2	L9.5 ± 1.2	0.06 ± 0.24	87%	No	Thick clouds?

Notes.
[a] Confidence limit; see Section 4.2.
[b] *HST*/WFPC2 observations in the F1042M band by Gizis et al. (2003) did not have sufficient sensitivity to detect any putative T dwarf secondary in this system.

5.2.8. SDSS J205235.31−160929.8

Chiu et al. (2006) classified SDSS J2052−1609 a T1 ± 1 (our SpeX classification is T0 ± 1), the uncertainty arising in part from strong absorption at 1.1 μm as compared to weak H_2O and CH_4 features at longer wavelengths. Despite satisfying only two selection criteria, this source appears to be a strong binary candidate, as the best-fit composite is a subtle but significantly better match to the data than the best-fit single template. Average component types of L7.5 ± 0.6 and T2 ± 0.2 are similar to those of SDSS J0423–0414, although in this case the secondary is inferred to be slightly brighter than its primary at the 1.05 μm and 1.27 μm spectral peaks ($\Delta J = 0.04 \pm 0.18$). The components of the best-fit composite, SDSS J1155−0559 (L7; 2MASS $J - K_s = 1.54 \pm 0.11$) and 2MASS J1122−3512 (T2; 2MASS $J - K_s = 0.64 \pm 0.08$), both have unusually blue near-infrared colors for their respective spectral types ($\langle J - K_s \rangle$ = 1.81 and 1.02 for L7 and T2 dwarfs, respectively; Faherty et al. 2009), suggesting that SDSS J2052−1609 may be an older or slightly metal-poor system. Indeed, its large proper motion (μ = 0.″483 ± 0.″022 yr^{-1}; J. Faherty 2010, in preparation) implies a fairly large tangential velocity ($V_{tan} = 48 \pm 8$ km s^{-1}), even without accounting for unresolved multiplicity in the photometric distance estimate (21 ± 3 pc). No high angular resolution imaging observations of this source have been reported to date.

5.2.9. Summary

Based on our analysis, we find that 17 of the 20 binary candidates identified by our spectral index selection criteria have a high probability of being (as yet) unresolved binaries, as indicated by the statistically significant better fits provided by composites. These include all of our strong candidates but only 63% (5/8) of our weak candidates, suggesting that at least three index selection criteria are preferred to identify robust binary candidates. The inferred properties of these systems are summarized in Table 10. The 12 systems with component types between L7 and T5 more than doubles the number of known binaries whose components span the L dwarf/T dwarf transition,[15] although we emphasize that these systems remain candidates pending verification via high angular resolution imaging and/or high resolution spectroscopic monitoring.

[15] Known or suspected L/T transition binaries include the six sources listed in Table 3 plus 2MASS J0850+1057 (Reid et al. 2001b; Dahn et al. 2002), 2MASS J0920+3517 (Reid et al. 2001b; Burgasser et al. 2006b), 2MASS J1728+3948 (Gizis et al. 2003), ϵ Indi BC (McCaughrean et al. 2004), and Gliese 337CD (Burgasser et al. 2005a).

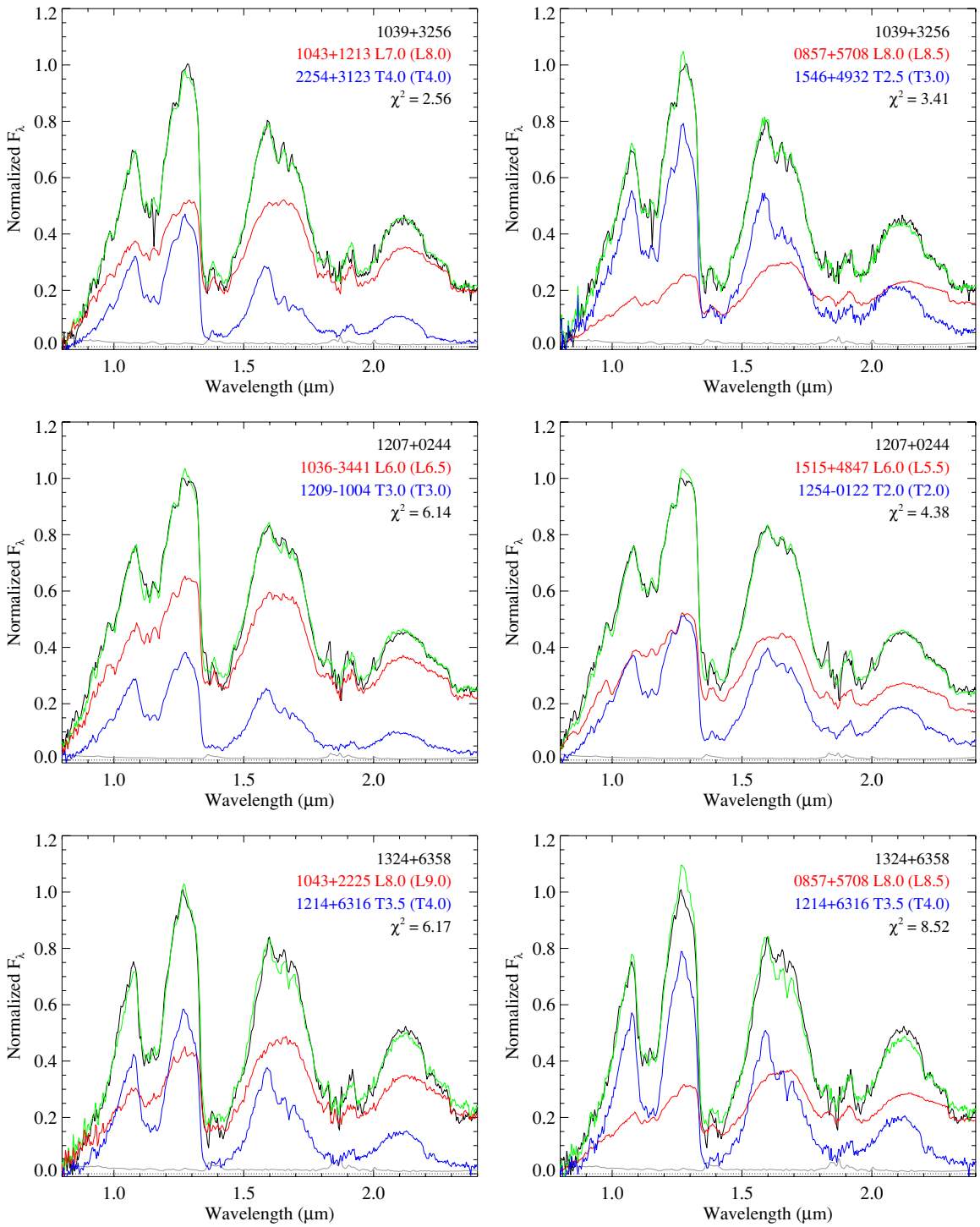

Figure 8. Spectral fits for SDSS J1039+3256 (top), SDSS J1207+0244 (middle), and 2MASS J1324+6358 (bottom) based on flux calibrations with the faint (left) or bright (right) absolute magnitude relations of Liu et al. (2006). These were the only three sources for which the two relations gave statistically distinct χ^2 residuals. Format is the same as the right panels in Figures 6 and 7.

(A color version of this figure is available in the online journal.)

6. DISCUSSION

6.1. Absolute Magnitudes Across the L Dwarf/T Dwarf Transition

As discussed in Section 1, there remains considerable uncertainty in absolute magnitude trends across the L dwarf/T dwarf transition due to the presence of unresolved multiples, gravity and metallicity effects, and ultimately the behavior of condensate clouds as they disperse out of the photosphere. With a large number of candidate binaries in our sample whose components straddle this transition, we considered whether it was possible to use these systems to better constrain the trends.

We first considered the quality of fits provided by the composites for the two flux calibration relations of Liu et al. (2006), which differ by nearly a full magnitude between types L7 and T5. For the 17 sources identified as promising binary candidates, we find that for 65% (11/17) of these the bright relation provides a lower χ^2 value for the best-fit composite (the same fraction is derived whether literature or index-based classifications are used). However, for only one case—SDSS J1207+0244—does the bright relation provide a statistically significant better fit; i.e., CL > 99% in the ratio of minimum χ^2 values between the best-fit composites for the bright and faint relations. On the other hand, for SDSS J1039+3256 and 2MASS J1324+6358 the bright relation provides a statistically significant *worse* fit (CL < 1%). Figure 8 compares the best-fit composites based on both faint and bright flux calibrations for these three sources, and indeed the lower χ^2 fits are clear improvements. All three of these systems also contain a T2–T4 secondary, within the spectral type range where the faint and bright relations of Liu et al. (2006) differ the most. Given the inconsistency in which relation provides better fits for our candidate binaries, we cannot definitely select one over the other on this analysis alone.

A more direct assessment can be made by focusing on individual brown dwarfs (singles and binary components) with parallax distance measurements. Figure 9 displays absolute MKO J magnitudes[16] for 58 L and T dwarfs with measured parallaxes and absolute magnitude errors $\leqslant$0.3 mag. Eighteen of these sources are known binaries; we include component magnitudes of the only candidate binary in our sample with a parallax measurement, 2MASS J1711+2232, along with measured component magnitudes for SDSS J0423-0414, SDSS J1021−0304, and ϵ Indi BC (McCaughrean et al. 2004). Nearly all of the unresolved sources and binary components follow the faint M_J relation up to spectral type ~T2; only the L9.5 2MASS J0328+2302 stands out as clearly overluminous in this range, with M_J magnitudes comparable to combined light photometry for Gliese 337CD. Between types T2 and T5, there are only two unresolved sources with parallax measurements, SDSS J1750+1759 (T3.5) and 2MASS J0559−1404 (T4.5), both of which lie well above the faint relation; indeed, the latter lies ~0.6 mag above the *bright* M_J relation. This could indicate a dramatic brightening over this spectral type range, as suggested by the component brightnesses of the resolved binary 2MASS J1404+3159 (Looper et al. 2008a) and our unresolved candidate SDSS J0119+2403 (Section 5.2.1). On the other hand, SDSS J1750+1759 and 2MASS J0559-1404 have both been suggested as unresolved multiples (Golimowski et al. 2004; Liu et al. 2006; Stephens et al. 2009), although neither satisfy any of our selection criteria. We therefore cannot rule out the possibility that they are young or otherwise peculiar sources.

The paucity of absolute magnitude measurements in the T2–T5 range makes it impossible to determine at this point whether absolute J magnitudes remain relatively flat across the entire L/T transition (a "J-band plateau;" Liu et al. 2006), favoring of modest flux reversal and more gradual cloud depletion; or undergo a sharp increase over types T2–T5 (a "J-band spike;" Looper et al. 2008a), requiring very rapid cloud depletion. Indeed, neither of these scenarios may encompass the behavior of all brown dwarfs. Increasing the number of T2–T5 dwarfs with parallax measurements, and obtaining resolved photometry of the candidates presented here, are both necessary if we are to properly constrain trends and distributions of absolute magnitudes across the L/T transition.

[16] Photometry shown in Figure 9 is based either on direct measurements (Geballe et al. 2002; Leggett et al. 2002; Knapp et al. 2004; Chiu et al. 2006) or synthetic filter corrections from 2MASS photometry as computed directly from the SpeX data; see Section 4.4.

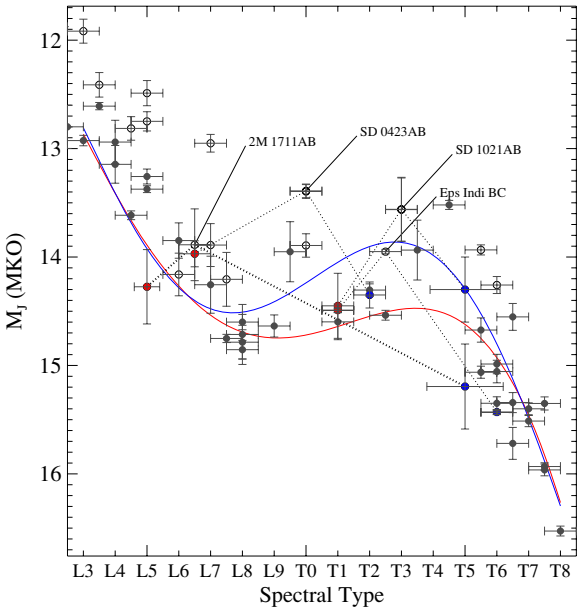

Figure 9. Absolute MKO J magnitudes vs. spectral type for L and T dwarfs with parallax measurements. Spectral types are based on optical classifications for L2–L8 dwarfs (Kirkpatrick et al. 1999) and near-infrared classifications for L9–T8 dwarfs (Burgasser et al. 2006b). Known multiples (including the candidate 2MASS J1711+2232) and unresolved sources with absolute magnitude uncertainties $\leqslant$0.3 mag are indicated as open and filled circles, respectively. Absolute magnitudes for the primary (red) and secondary (blue) components of SDSS J0423–0414, SDSS J1021−0304, 2MASS J1711+2232, and ϵ Indi BC (McCaughrean et al. 2004; Burgasser et al. 2006c; this paper) are also indicated by filled circles and connected to their combined-light magnitude and spectral types (dotted lines). The bright (top) and faint (bottom) absolute magnitude relations of Liu et al. (2006) are delineated by solid blue and red lines, respectively.

(A color version of this figure is available in the online journal.)

6.2. The Frequency of Brown Dwarf Binaries

Higher rates of multiplicity among early-type T dwarfs have been observed in resolved imaging studies (Burgasser et al. 2006c), although statistics in these samples remain poor due to small numbers (Goldman et al. 2008). As our candidate sample includes sources that might be undetectable in high resolution imaging, it is relevant to assess how their inclusion in multiplicity statistics modifies brown dwarf binary fraction trends across the L/T transition, and what constraint can be made on the intrinsic binary fraction.

As discussed in Section 2, our spectral sample is neither complete nor volume-limited, and selection biases are uncertain given that sources were identified from different search programs using different color and magnitude selection criteria. However, as a first approach we made the simplifying assumption that the sample is roughly magnitude-limited, and estimated the fraction of L8–T6 dwarfs with SpeX data that are either resolved or candidate binaries. These numbers are summarized in Table 11, and indicate the same high multiplicity rate among early-type T dwarfs as found in resolved imaging studies. For T0–T4 dwarfs, we deduce a binary fraction of 53% ± 7% (23/43 sources), peaking above 60% for T0–T2 dwarfs alone. Over half of the early-type T dwarfs in this spectral sample appear to

Table 11
Estimated Binary Fractions for SpeX Sample

SpT	Number of Sources				Binary Fraction[a]	
	Total	Resolved	Candidates	Non-candidates	Observed	Predicted[b]
(1)	(2)	(3)	(4)	(5)	(6)	(7)
L8–L9	12	0	0	12	<13%	33%
L9–T0	9	1	0	8	11^{+18}_{-4}%	49%
T0–T1	9	3	3	3	67^{+11}_{-17}%	70%
T1–T2	10	1	5	4	60^{+13}_{-16}%	68%
T2–T3	17	1	7	9	47^{+12}_{-11}%	45%
T3–T4	7	2	1	4	43^{+18}_{-15}%	23%
T4–T5	10	1	0	9	10^{+17}_{-3}%	26%
T5–T6	20	1	0	19	5^{+10}_{-2}%	30%
T0–T4	43	7	16	20	53 ± 7%	56%

Notes.
[a] Including resolved binaries plus binary candidates.
[b] Based on the simulations of Burgasser (2007a), assuming a mass function $\Psi(M) \propto M^{-0.5}$, a constant birthrate over 0.01 Gyr $< t <$ 10 Gyr, an intrinsic binary fraction $\epsilon_b = 15\%$, a mass ratio distribution $P(q) \propto q^4$, evolutionary models from Baraffe et al. (2003), *K*-band absolute magnitude and bolometric magnitude relations as defined in that study, and a magnitude-limited sample.

be multiples, compared to ∼30% in resolved imaging samples (Burgasser 2007a). Moreover, the fraction inferred here is likely to be a lower limit, given that we are unable to identify unresolved binaries with identical components or combinations that fall outside our spectral index selection criteria (see Section 3.2).

Such a high *apparent* rate of multiplicity does not necessary translate into a high *intrinsic* (i.e., volume-limited) rate, however. As discussed in Burgasser (2007a), the enhanced binary fraction of early-type T dwarfs arises predominantly from the small change in luminosity across the L dwarf/T dwarf transition, which induces both a sharp minimum in the luminosity function of brown dwarfs at type T0 (roughly three times rarer in number than early- and mid-type L dwarfs) and makes late-type L and early-type T dwarfs comparably bright in the near-infrared. Combined with the preferential selection of binaries in magnitude-limited samples, these effects collude to amplify the apparent multiplicity rate of early-type T dwarfs. To infer the intrinsic rate, we reproduced the Monte Carlo population simulations of Burgasser (2007a), using the baseline parameters defined in that study and assuming a magnitude-limited sample. We find that an intrinsic rate of only 15% can produce an apparent binary fraction of 56% for T0–T4 dwarfs in a magnitude-limited sample, comparable to the fraction estimated above. This intrinsic rate is in fact on the low end of current estimates that attempt to correct for unresolved multiplicity (e.g., Basri & Reiners 2006; Lodieu et al. 2007; Joergens 2008), and remains consistent with a brown dwarf multiplicity fraction that is significantly lower than those of more massive stars (e.g., Duquennoy & Mayor 1991; Fischer & Marcy 1992). We reiterate, however, that our result constitutes a lower limit, and a robust measure requires detailed modeling of selection effects (e.g., component spectral type sensitivity range, mass ratio sensitivity as a function of age) that are beyond the scope of this paper.

6.3. Flux Reversals and Cloud Evolution

The physical feature that ties both absolute magnitude trends and enhanced binary fractions across the L/T transition is the "sudden" depletion of condensate clouds from the photosphere. This is particularly evident in the increased surface fluxes at the 1.05 μm and 1.27 μm flux peaks where cloud particles are a dominant source of opacity (Ackerman & Marley 2001). Among the binary candidates identified here, 59% (10/17) of the entire sample and 82% (9/11) of candidates with L7–T5 components show similar flux reversals in the *J*-band region. While these reversals are dictated in part by our adopted flux calibration (which are, however, tied to the *K*-band flux; see Section 4.1), the quality of the fits coupled with observed absolute magnitude/spectral type trends (Section 6.1) suggest that these flux reversals are real.

With a relatively large sample of possible L dwarf/T dwarf pairs, we can also assess how these flux reversals vary between systems with similar spectral compositions. Consider the candidates SDSS J0119+2403 and SDSS J1106+2754, which have component types of T0+T4 and T0+T4.5 and relative brightnesses of $\Delta J = -0.42 \pm 0.19$ and -0.37 ± 0.06, respectively. Examination of the best-fit composites for these sources (Figures 6 and 7) reveals that the former has a far more pronounced flux reversal than the latter, with the secondary of SDSS J0119+2403 being potentially brighter even at the 1.6 μm flux peak. The best-fit primary of this system was inferred to be an unusually cloudy source, which translates in greater opacity in the *J*-band region. In contrast, the primary of 2MASS J1106+2754 was inferred to be slightly blue for its spectral type, which could be attributed to thinner condensate clouds (e.g., Knapp et al. 2004; Burgasser et al. 2008b). If clouds are the main driver for the unusual colors of the primary components, and their secondaries are roughly equivalent, the different flux reversals can be tied directly to variations in cloud properties. Specifically, an initially cloudy brown dwarf should lose more opacity in the *J*-band region, and experience a greater increase in brightness, as it evolves across the L/T transition as compared to a brown dwarf that initially has thinner clouds. This correlation between initial cloud content and degree of flux reversal suggests that absolute magnitude trends may have more spread across the L/T transition than can be discerned in the currently sparse data set; spread has also been suggested to arise from age/surface gravity effects (e.g., Metchev & Hillenbrand 2006; Mohanty et al. 2007) and metallicity variations (e.g., Burrows et al. 2006). Again, resolved studies of confirmed binaries in our sample would provide insight into how atmospheric properties modulate the removal of condensate clouds.

6.4. Limitations of this Study

Despite the large number of potential L dwarf/T dwarf pairs uncovered in this investigation, there are clearly limitations as pertaining to the completeness of the sample and robustness of the component characterizations. We reiterate that the 17 candidates listed in Table 10 may not represent the full complement of potential binaries in our spectral sample. Our selection criteria were specifically chosen to be conservative so as to not eliminate too many spectral templates, particularly over the L8–T5 spectral type range. As such, we failed to select known binary systems with early-type T dwarf classifications (Section 3.2) and a number of suspected binary pairs such as 2MASS J0328+2302. We are also unable to select systems with similar spectral component types, and are likely biased against higher-order multiples such as Kelu 1 (Stumpf et al. 2008) and DENIS-P J020529.0–115925 (Bouy et al. 2005). The retention of unresolved binaries in our template sample may also skew the statistical significance of our candidates. For instance, our

rejected candidate SDSS J1206+2813, whose spectrum is a near clone to that of SDSS J1750+1759, may prove to be a binary after all should the latter be determined as such. On the other hand, incomplete sampling of single L dwarf/T dwarf transition objects in our spectral template library may cause us to over-select candidates, a possibility for the poorly fit candidate 2MASS J2139+0220. It is in this vein that we encourage follow-up high resolution imaging (or second epoch imaging in the cases of 2MASS J1106+2754 and 2MASS J1711+2232) and spectroscopy of the candidates listed in Table 10 to both verify their binary nature and better characterize their components.

7. SUMMARY

We have identified 17 candidate brown dwarf binaries whose components straddle the L dwarf/T dwarf transition. Their unresolved multiplicity is inferred from similarities in near-infrared spectral indices to known binary systems, and statistically significant better fits to near-infrared spectra by composite templates as compared to single templates. Ten of these systems appear to have secondaries that are brighter than their primaries over the 1–1.3 μm region, by up to $\sim$0.4 mag, consistent with a nonequilibrium depletion of condensate clouds across the L dwarf/T dwarf transition. This is despite the fact that our analysis of these systems is based largely on the faint absolute magnitude relations of Liu et al. (2006). We cannot rule out an even more pronounced *J*-band flux reversal for the sparsely sampled T3–T5 dwarfs. We find that 53% $\pm$ 7% of the T0–T4 dwarfs in our SpeX spectral sample are resolved or unresolved (candidate) binaries, a rate that is consistent with an intrinsic brown dwarf binary fraction of at least 15%, assuming the sample is magnitude-limited. We find some evidence of flux reversal variations between similarly classified pairs that may arise from cloud effects, although these must be verified through more accurate characterization of the components. While the sample of candidate binaries presented here does require verification through follow-up high resolution imaging and/or spectroscopic monitoring, it constitutes a promising collection of coeval laboratories for understanding the atmospheric processes that drive the still poorly understood L dwarf/T dwarf transition.

The authors thank telescope operators Bill Golisch, Dave Griep, and Paul Sears, and instrument specialist John Rayner, for their assistance during our many IRTF runs. The authors also thank the anonymous referee for her/his review of the manuscript. This publication makes use of data from the Two Micron All Sky Survey, which is a joint project of the University of Massachusetts and the Infrared Processing and Analysis Center, and funded by the National Aeronautics and Space Administration and the National Science Foundation. 2MASS data were obtained from the NASA/IPAC Infrared Science Archive, which is operated by the Jet Propulsion Laboratory, California Institute of Technology, under contract with the National Aeronautics and Space Administration. This research has also made use of the SIMBAD database, operated at CDS, Strasbourg, France; the M, L, and T dwarf compendium housed at DwarfArchives.org and maintained by Chris Gelino, Davy Kirkpatrick, and Adam Burgasser; the SpeX Prism Spectral Libraries, maintained by Adam Burgasser at http://www.browndwarfs.org/spexprism; and the VLM Binaries Archive maintained by Nick Siegler at http://www.vlmbinaries.org. The authors wish to recognize and acknowledge the very significant cultural role and reverence that the summit of Mauna Kea has always had within the indigenous Hawaiian community. We are most fortunate to have the opportunity to conduct observations from this mountain.

Facilities: IRTF (SpeX)

REFERENCES

Ackerman, A. S., & Marley, M. S. 2001, ApJ, 556, 872
Allen, P. R. 2007, ApJ, 668, 492
Artigau, É., Doyon, R., Lafrenière, D., Nadeau, D., Robert, J., & Albert, L. 2006, ApJ, 651, L57
Baraffe, I., Chabrier, G., Barman, T. S., Allard, F., & Hauschildt, P. H. 2003, A&A, 402, 701
Basri, G., & Martín, E. L. 1999, AJ, 118, 2460
Basri, G., & Reiners, A. 2006, AJ, 132, 663
Blake, C. H., Charbonneau, D., White, R. J., Torres, G., Marley, M. S., & Saumon, D. 2008, ApJ, 678, L125
Bouy, H., Martín, E. L., Brandner, W., & Bouvier, J. 2005, AJ, 129, 511
Burgasser, A. J. 2007a, ApJ, 659, 655
Burgasser, A. J. 2007b, AJ, 134, 1330
Burgasser, A. J. 2007c, ApJ, 658, 617
Burgasser, A. J., Burrows, A., & Kirkpatrick, J. D. 2006a, ApJ, 639, 1095
Burgasser, A. J., Geballe, T. R., Leggett, S. K., Kirkpatrick, J. D., & Golimowski, D. A. 2006b, ApJ, 637, 1067
Burgasser, A. J., Kirkpatrick, J. D., Cruz, K. L., Reid, I. N., Leggett, S. K., Liebert, J., Burrows, A., & Brown, M. E. 2006c, ApJS, 166, 585
Burgasser, A. J., Kirkpatrick, J. D., Liebert, J., & Burrows, A. 2003a, ApJ, 594, 510
Burgasser, A. J., Kirkpatrick, J. D., & Lowrance, P. J. 2005a, AJ, 129, 2849
Burgasser, A. J., Kirkpatrick, J. D., McElwain, M. W., Cutri, R. M., Burgasser, A. J., & Skrutskie, M. F. 2003b, AJ, 125, 850
Burgasser, A. J., Liu, M. C., Ireland, M. J., Cruz, K. L., & Dupuy, T. J. 2008a, ApJ, 681, 579
Burgasser, A. J., Looper, D. L., Kirkpatrick, J. D., Cruz, K. L., & Swift, B. J. 2008b, ApJ, 674, 451
Burgasser, A. J., Looper, D. L., Kirkpatrick, J. D., & Liu, M. C. 2007a, ApJ, 658, 557
Burgasser, A. J., & McElwain, M. W. 2006, AJ, 131, 1007
Burgasser, A. J., McElwain, M. W., & Kirkpatrick, J. D. 2003c, AJ, 126, 2487
Burgasser, A. J., McElwain, M. W., Kirkpatrick, J. D., Cruz, K. L., Tinney, C. G., & Reid, I. N. 2004, AJ, 127, 2856
Burgasser, A. J., Reid, I. N., Leggett, S. K., Kirkpatrick, J. D., Liebert, J., & Burrows, A. 2005b, ApJ, 634, L177
Burgasser, A. J., Reid, I. N., Siegler, N., Close, L., Allen, P., Lowrance, P., & Gizis, J. 2007b, in Protostars and Planets V, ed. B. Reipurth, D. Jewitt, & K. Keil (Tucson, AZ: Univ. Arizona Press), 427
Burgasser, A. J., et al. 1999, ApJ, 522, L65
Burgasser, A. J., et al. 2000a, AJ, 120, 1100
Burgasser, A. J., et al. 2000b, ApJ, 531, L57
Burgasser, A. J., et al. 2002a, ApJ, 564, 421
Burgasser, A. J., et al. 2002b, ApJ, 571, L151
Burgasser, A. J., et al. 2003d, ApJ, 592, 1186
Burrows, A., Sudarsky, D., & Hubeny, I. 2006, ApJ, 640, 1063
Chabrier, G., Baraffe, I., Leconte, J., Gallardo, J., & Barman, T. 2009, in AIP Conf. Ser. 1094, Cool Stars, Stellar Systems and the Sun, ed. E. Stempels (Melville, NY: AIP), 102
Chiu, K., Fan, X., Leggett, S. K., Golimowski, D. A., Zheng, W., Geballe, T. R., Schneider, D. P., & Brinkmann, J. 2006, AJ, 131, 2722
Cruz, K. L., Burgasser, A. J., Reid, I. N., & Liebert, J. 2004, ApJ, 604, L61
Cruz, K. L., Kirkpatrick, J. D., & Burgasser, A. J. 2009, AJ, 137, 3345
Cruz, K. L., Reid, I. N., Liebert, J., Kirkpatrick, J. D., & Lowrance, P. J. 2003, AJ, 126, 2421
Cruz, K. L., et al. 2007, AJ, 133, 439
Cushing, M. C., Rayner, J. T., & Vacca, W. D. 2005, ApJ, 623, 1115
Cushing, M. C., Vacca, W. D., & Rayner, J. T. 2004, PASP, 116, 362
Cushing, M. C., et al. 2006, ApJ, 648, 614
Cushing, M. C., et al. 2008, ApJ, 678, 1372
Dahn, C. C., et al. 2002, AJ, 124, 1170
Delfosse, X., et al. 1997, A&A, 327, L25
Dupuy, T. J., Liu, M. C., & Ireland, M. J. 2009, ApJ, 692, 729
Duquennoy, A., & Mayor, M. 1991, A&A, 248, 485
Ellis, S. C., Tinney, C. G., Burgasser, A. J., Kirkpatrick, J. D., & McElwain, M. W. 2005, AJ, 130, 2347
Epchtein, N., et al. 1997, The Messenger, 87, 27
Faherty, J. K., Burgasser, A. J., Cruz, K. L., Shara, M. M., Walter, F. M., & Gelino, C. R. 2009, AJ, 137, 1

Fan, X., et al. 2000, AJ, 119, 928
Fischer, D. A., & Marcy, G. W. 1992, ApJ, 396, 178
Geballe, T. R., et al. 2002, ApJ, 564, 466
Gelino, C. R., Kulkarni, S. R., & Stephens, D. C. 2006, PASP, 118, 611
Gizis, J. E. 2002, ApJ, 575, 484
Gizis, J. E., Monet, D. G., Reid, I. N., Kirkpatrick, J. D., Liebert, J., & Williams, R. J. 2000, AJ, 120, 1085
Gizis, J. E., Reid, I. N., Knapp, G. R., Liebert, J., Kirkpatrick, J. D., Koerner, D. W., & Burgasser, A. J. 2003, AJ, 125, 3302
Goldman, B., Bouy, H., Zapatero Osorio, M. R., Stumpf, M. B., Brandner, W., & Henning, T. 2008, A&A, 490, 763
Golimowski, D. A., et al. 2004, AJ, 127, 3516
Hawley, S. L., et al. 2002, AJ, 123, 3409
Joergens, V. 2008, A&A, 492, 545
Joergens, V., & Müller, A. 2007, ApJ, 666, L113
Kendall, T. R., Delfosse, X., Martín, E. L., & Forveille, T. 2004, A&A, 416, L17
Kendall, T. R., Jones, H. R. A., Pinfield, D. J., Pokorny, R. S., Folkes, S., Weights, D., Jenkins, J. S., & Mauron, N. 2007, MNRAS, 374, 445
Kendall, T. R., Mauron, N., Azzopardi, M., & Gigoyan, K. 2003, A&A, 403, 929
Kirkpatrick, J. D. 2005, ARA&A, 43, 195
Kirkpatrick, J. D., et al. 1999, ApJ, 519, 802
Kirkpatrick, J. D., et al. 2000, AJ, 120, 447
Kirkpatrick, J. D., et al. 2008, ApJ, 689, 1295
Knapp, G. R., et al. 2004, AJ, 127, 3553
Leggett, S. K., Saumon, D., Marley, M. S., Geballe, T. R., Golimowski, D. A., Stephens, D., & Fan, X. 2007, ApJ, 655, 1079
Leggett, S. K., et al. 2000, ApJ, 536, L35
Leggett, S. K., et al. 2002, ApJ, 564, 452
Liebert, J., & Burgasser, A. J. 2007, ApJ, 655, 522
Liebert, J., & Gizis, J. E. 2006, PASP, 118, 659
Liebert, J., Kirkpatrick, J. D., Cruz, K. L., Reid, I. N., Burgasser, A., Tinney, C. G., & Gizis, J. E. 2003, AJ, 125, 343
Liu, M. C., Dupuy, T. J., & Ireland, M. J. 2008, ApJ, 689, 436
Liu, M. C., & Leggett, S. K. 2005, ApJ, 634, 616
Liu, M. C., Leggett, S. K., Golimowski, D. A., Chiu, K., Fan, X., Geballe, T. R., Schneider, D. P., & Brinkmann, J. 2006, ApJ, 647, 1393
Lodders, K. 2002, ApJ, 577, 974
Lodieu, N., Dobbie, P. D., Deacon, N. R., Hodgkin, S. T., Hambly, N. C., & Jameson, R. F. 2007, MNRAS, 380, 712
Looper, D. L., Gelino, C. R., Burgasser, A. J., & Kirkpatrick, J. D. 2008a, ApJ, 685, 1183
Looper, D. L., Kirkpatrick, J. D., & Burgasser, A. J. 2007, AJ, 134, 1162
Looper, D. L., et al. 2008b, ApJ, 686, 528
Lucas, P. W., & Roche, P. F. 2000, MNRAS, 314, 858
Luhman, K. L., et al. 2007, ApJ, 654, 570
Marley, M. S., Saumon, D., Guillot, T., Freedman, R. S., Hubbard, W. B., Burrows, A., & Lunine, J. I. 1996, Science, 272, 1919
Martín, E. L., Brandner, W., & Basri, G. 1999a, Science, 283, 1718
Martín, E. L., Delfosse, X., Basri, G., Goldman, B., Forveille, T., & Zapatero Osorio, M. R. 1999b, AJ, 118, 2466
McCaughrean, M. J., Close, L. M., Scholz, R.-D., Lenzen, R., Biller, B., Brandner, W., Hartung, M., & Lodieu, N. 2004, A&A, 413, 1029
McElwain, M. W., & Burgasser, A. J. 2006, AJ, 132, 2074
McLean, I. S., McGovern, M. R., Burgasser, A. J., Kirkpatrick, J. D., Prato, L., & Kim, S. S. 2003, ApJ, 596, 561
Metchev, S. A., & Hillenbrand, L. A. 2006, ApJ, 651, 1166
Metchev, S. A., Kirkpatrick, J. D., Berriman, G. B., & Looper, D. 2008, ApJ, 676, 1281
Mohanty, S., Jayawardhana, R., Huélamo, N., & Mamajek, E. 2007, ApJ, 657, 1064
Muench, A. A., Lada, C. J., Luhman, K. L., Muzerolle, J., & Young, E. 2007, AJ, 134, 411
Mugrauer, M., Seifahrt, A., Neuhäuser, R., & Mazeh, T. 2006, MNRAS, 373, L31
Nakajima, T., Tsuji, T., & Yanagisawa, K. 2004, ApJ, 607, 499
Rayner, J. T., Toomey, D. W., Onaka, P. M., Denault, A. J., Stahlberger, W. E., Vacca, W. D., Cushing, M. C., & Wang, S. 2003, PASP, 115, 362
Reid, I. N., Burgasser, A. J., Cruz, K. L., Kirkpatrick, J. D., & Gizis, J. E. 2001a, AJ, 121, 1710
Reid, I. N., Cruz, K. L., Kirkpatrick, J. D., Allen, P. R., Mungall, F., Liebert, J., Lowrance, P., & Sweet, A. 2008, AJ, 136, 1290
Reid, I. N., Gizis, J. E., Kirkpatrick, J. D., & Koerner, D. W. 2001b, AJ, 121, 489
Reid, I. N., Kirkpatrick, J. D., Gizis, J. E., Dahn, C. C., Monet, D. G., Williams, R. J., Liebert, J., & Burgasser, A. J. 2000, AJ, 119, 369
Reid, I. N., Lewitus, E., Burgasser, A. J., & Cruz, K. L. 2006, ApJ, 639, 1114
Saumon, D., & Marley, M. S. 2008, ApJ, 689, 1327
Schneider, D. P., et al. 2002, AJ, 123, 458
Sheppard, S. S., & Cushing, M. C. 2009, AJ, 137, 304
Siegler, N., Close, L. M., Burgasser, A. J., Cruz, K. L., Marois, C., Macintosh, B., & Barman, T. 2007, AJ, 133, 2320
Simons, D. A., & Tokunaga, A. 2002, PASP, 114, 169
Skrutskie, M. F., et al. 2006, AJ, 131, 1163
Stassun, K. G., Mathieu, R. D., & Valenti, J. A. 2006, Nature, 440, 311
Stephens, D. C., et al. 2009, ApJ, 702, 154
Strauss, M. A., et al. 1999, ApJ, 522, L61
Stumpf, M. B., Brandner, W., Köhler, R., Bouy, H., & Henning, Th. 2009, in AIP Conf. Proc. 1094, Cool Stars, Stellar Systems and the Sun, ed. E. Stempels (Melville, NY: AIP), 561
Testi, L., et al. 2001, ApJ, 552, L147
Tinney, C. G., Burgasser, A. J., & Kirkpatrick, J. D. 2003, AJ, 126, 975
Tinney, C. G., Burgasser, A. J., Kirkpatrick, J. D., & McElwain, M. W. 2005, AJ, 130, 2326
Tokunaga, A. T., Simons, D. A., & Vacca, W. D. 2002, PASP, 114, 180
Tsuji, T. 2002, ApJ, 575, 264
Tsuji, T. 2005, ApJ, 621, 1033
Tsuji, T., & Nakajima, T. 2003, ApJ, 585, L151
Tsuji, T., Nakajima, T., & Yanagisawa, K. 2004, ApJ, 607, 511
Tsuji, T., Ohnaka, K., & Aoki, W. 1996, A&A, 305, L1
Tsuji, T., Ohnaka, K., & Aoki, W. 1999, ApJ, 520, L119
Tsvetanov, Z. I., et al. 2000, ApJ, 531, L61
Vacca, W. D., Cushing, M. C., & Rayner, J. T. 2003, PASP, 115, 389
Vrba, F. J., et al. 2004, AJ, 127, 2948
Wilson, J. C., Miller, N. A., Gizis, J. E., Skrutskie, M. F., Houck, J. R., Kirkpatrick, J. D., Burgasser, A. J., & Monet, D. G. 2003, in IAU Symp. 211, Brown Dwarfs, ed. E. Martín (Dordrecht: Kluwer), 197
York, D. G., et al. 2000, AJ, 120, 1579
Zapatero Osorio, M. R., Lane, B. F., Pavlenko, Y., Martín, E. L., Britton, M., & Kulkarni, S. R. 2004, ApJ, 615, 958